The Cryosphere
Discussions
Open Access
EGU

Measurement of Ice Shelf Rift Width with ICESat-2 Laser Altimetry: Automation, Validation, and the Behavior of Halloween Crack, Brunt Ice Shelf, East Antarctica

Ashley Morris[1], Bradley P. Lipovsky[1], Catherine C. Walker[2], and Oliver J. Marsh[3]

[1]Department of Earth and Space Sciences, University of Washington, Johnson Hall, 4000 15th Avenue NE, Seattle, WA 98195-1310, United States of America
[2]Woods Hole Oceanographic Institution, 266 Woods Hole Road, Woods Hole, MA 02543-1050, United States of America
[3]British Antarctic Survey, High Cross, Madingley Road, Cambridge CB3 0ET, United Kingdom

Correspondence: Ashley Morris (richard.ashley.morris@gmail.com)

Abstract. Ice shelves influence the mass balance of the Antarctic Ice Sheet by restricting the flow of ice across the grounding zone. Their ability to restrict ice flow is sensitive to changes in their extent or thickness. Full thickness fractures, known as rifts, create tabular icebergs which reduce ice shelf extent. We present a method for measuring rift width using ICESat-2 laser altimetry, as part of a larger effort to detect, catalog and measure various characteristics of Antarctic rifts. We validate the

5 results using optical satellite imagery and data from Global Navigation Satellite System (GNSS) receivers around "Halloween Crack" on Brunt Ice Shelf, East Antarctica. During the study period a further rift, "North Rift" formed and rapidly calved a $\sim$1270 km^2 iceberg. In response to this second rift, the opening of Halloween Crack approached stagnation before returning to opening at a reduced rate. We suggest the opening rate is controlled by the ice shelf geometry and degree of contact with a pinning point at McDonald Ice Rumples, and its influence on the large-scale ice flow field. We replicate the general pattern

10 of opening using an inverse finite element model, and discuss the response of the ice shelf to the calving. We use historical satellite imagery and previously published ice-front positions to demonstrate the importance of McDonald Ice Rumples to the long-term calving and advance cycle of Brunt Ice Shelf.

1 Introduction

The Antarctic Ice Sheet gains mass through the accumulation of snowfall and loses mass primarily where it comes into contact

15 with the ocean. Floating ice shelves fringe 75 % of the ice sheet margin (Rignot et al., 2013), buttressing the flow of ice streams inland (Dupont and Alley, 2005; Fürst et al., 2016) due to flow resistance at lateral boundaries, ice rises and ice rumples (Matsuoka et al., 2015). Ice shelves gain mass through the flow of ice across the grounding zone, snowfall, and potentially basal accretion, and lose mass through basal melting and iceberg calving. These mass loss processes occur in roughly equal proportions at the continental scale, but vary strongly regionally (Rignot et al., 2013; Depoorter et al., 2013; Greene et al., 2022).

20 Where mass losses exceed mass gains, ice shelves retreat and/or thin, reducing buttressing and increasing the flow speed of grounded ice (Scambos et al., 2004; Rott et al., 2011; Joughin et al., 2021; MacGregor et al., 2012; Pritchard et al., 2012; Mouginot et al., 2014; Gudmundsson et al., 2019). Ice shelves thus exert a key control on Antarctic Ice Sheet mass balance and

global sea level variations (Fox-Kemper et al., 2021). Radar altimetry satellites have been used to map ice shelf topography and monitor thickness changes (Paolo et al., 2015; Zwally et al., 2005), however, their coarse spatial resolution has restricted

25 their use for examining processes occurring at smaller scales. Only with the launch of the first Ice, Cloud and Land Elevation Satellite (ICESat) laser altimeter was satellite altimetry applied to the study of the rifting and iceberg calving process (Fricker et al., 2005a).

Rifts are full thickness fractures through ice shelves which often form in ice shelf margins, the grounding zone, at the calving front, or near ice rises and ice rumples (Benn et al., 2007). A range of factors influencing rift propagation have been iden-

30 tified, including glaciological stresses (Walker et al., 2013; Joughin and MacAyeal, 2005; Hulbe et al., 2010; Bassis et al., 2005, 2007, 2008; Heeszel et al., 2014; Lipovsky, 2020; Olinger et al., 2022), the thickness and mechanical strength of ice mélange within rifts (Fricker et al., 2005b; Larour et al., 2004, 2021; MacAyeal et al., 1998; Rignot and MacAyeal, 1998), sea surface slopes driven by large-scale atmospheric conditions (Francis et al., 2021, 2022; Christie et al., 2022) or tides (Olinger et al., 2019), ocean waves and the concentration of protective sea ice (Massom et al., 2018; Christie et al., 2022; Cathles IV

35 et al., 2009; Aster et al., 2021; Bromirski et al., 2010; Bromirski and Stephen, 2012; MacAyeal et al., 2006; Banwell et al., 2017; Lipovsky, 2018), and Tsunami-generated swell (Walker et al., 2015, 2013; Brunt et al., 2011).

Walker et al. (2013) used moderate resolution satellite imagery to observe 78 rifts around the Antarctic continent between 2002 and 2012, finding a spectrum of decadal behavior from complete dormancy, through intermittent or sudden bursts of extension, to continuous activity. Detailed *in situ* and remote sensing studies of individual rifts or small numbers of rifts suggest that prop-

40 agation occurs as episodic short bursts lasting seconds (Banwell et al., 2017) to hours (Bassis et al., 2005, 2007), with opening widths increasing steadily (Joughin and MacAyeal, 2005). Propagation is often arrested or slowed at suture zones, where fracture toughness can be higher (Borstad et al., 2017; Hulbe et al., 2010; Bassis et al., 2007). Once rifts propagate sufficiently to intersect the ice shelf front or other rifts, tabular iceberg calving occurs. Ice shelves typically exhibit "calving cycles", with long periods of advance separating sequential large calving events (Fricker et al., 2002; Wang et al., 2022; Cheng et al., 2021a;

45 Giles, 2017). Although the calving cycle is commonly envisioned as a steady-state process on decadal timescales (Greene et al., 2022), recent studies have examined the degradation of regular calving cycles and the associated loss of grounded ice mass (Joughin et al., 2021). Greene et al. (2022) showed that since 1997 Antarctic ice shelves have exhibited comparable net ice losses due to calving ($5{,}874 \pm 396\,\mathrm{Gt}$) and basal melt ($6{,}113 \pm 452\,\mathrm{Gt}$), with modeling suggesting this resulted in similar reductions in ice shelf buttressing.

50 Launched in 2018, NASA's Ice, Cloud and Land Elevation Satellite-2 (ICESat-2) carries the Advanced Topographic Laser Altimeter System (ATLAS), a photon counting laser altimeter (see Sect. 3.1) which provides both extensive spatial coverage and fine spatial resolution (Markus et al., 2017; Abdalati et al., 2010). ICESat-2 is able to measure rift width and other parameters in the vertical dimension such as ice mélange thickness, seaward-landward offset (Walker and Gardner, 2019) and rift flank topography (Walker et al., 2021; Fricker et al., 2005a). In this paper we describe the measurement of a time series of rift widths

55 using ICESat-2 laser altimetry, and validation using other remote-sensing and field-based datasets, using "Halloween Crack" (HC) on Brunt Ice Shelf (BIS), East Antarctica as a case study (Fig. 1). We observe changes in the ice shelf flow field and changes in rift behavior following calving from "North Rift" (NR), which we investigate using remote sensing data and a finite

element ice flow model. We place these contemporary changes in a long-term perspective by examining the calving cycle at
BIS using historical remote sensing data and published observations.

60

2 Study area

BIS (75.3° S to 75.8° S, 24.0° W to 27.0° W), drains ice from Coats Land, East Antarctica into the Weddell Sea (Fig. 1). Ice
blocks which detach in the steeply sloping grounding zone are bound together by sea ice channels which become increasingly
filled by snow and firn as the ice advects through the shelf (King et al., 2018; Fretwell et al., 2013). Ice blocks from grounding
65 zone troughs are thicker and more closely packed than from adjacent shallower, slower flowing areas (King et al., 2018). The
ice shelf is grounded on a bathymetric high point called McDonald Ice Rumples (MIR), located at 75.44° S, 26.3° W. This
exerts a strong control on present ice flow (Figs. 1 and S1), past ice flow variability (Gudmundsson et al., 2017; De Rydt et al.,
2018, 2019) and stresses within the ice shelf (De Rydt et al., 2019).

The earliest observations of BIS date back to the 1914/15 voyage of HMS *Endurance*, thus capturing the entire calving cycle
70 (Fig. 2), albeit with low temporal resolution prior to the satellite period. In 1971 BIS calved back to a number of large rifts
which had formed in 1968 (Thomas, 1973; Gudmundsson et al., 2017). Measurements from across BIS show almost a doubling
in ice flow velocity in the 1970s, which was sustained through the 1980s and 1990s. More recent GPS measurements show
the velocity decreasing through the 2000s, reaching pre-1970s levels by ∼2010, with a further period of acceleration starting
in 2012 (Simmons and Rouse, 1984; Gudmundsson et al., 2017). Gudmundsson et al. (2017) modelled the impact on ice flow
75 velocity on the opening of a rift between BIS and adjacent Stancomb-Wills Ice Tongue (SWIT), the opening of the dormant
Chasm 1 rift which had formed in the grounding zone in the 1970s (De Rydt et al., 2018, 2019), and the loss of contact with
MIR following the 1971 calving. The closest match to the observed magnitude and pattern of velocity increase resulted from
the simulated loss of mechanical contact between BIS and the pinning point at MIR. Over the next three decades the ice shelf
gradually re-advanced, and by ∼1997 buttressing from MIR was sufficient for velocities to begin to decrease (Gudmundsson
80 et al., 2017; De Rydt et al., 2018). The reorganization of internal stresses resulting from the increase in buttressing from MIR
resulted in the reactivation of Chasm 1, potentially explaining the increase in velocity after 2012 (Gudmundsson et al., 2017). A
second major rift, Halloween Crack (HC), formed in October 2016, in a similar location to the rift from which the 1971 iceberg
calved (Thomas, 1973; De Rydt et al., 2018). HC propagated in both directions from a point approximately 15 km east of MIR,
slowing where it encountered thicker ice originating from the grounding zone troughs (De Rydt et al., 2018; King et al., 2018).
85 A third major rift, North Rift (NR), seaward of HC, was observed to be propagating in November 2020 (British Antarctic
Survey Press Office, 2021), resulting in the calving of a ∼1270 km^2 iceberg (A-74) in February 2021 (Francis et al., 2022;
Libert et al., 2022; Cheng et al., 2021b; British Antarctic Survey Press Office, 2021). A further ∼1550 km^2 iceberg (A-81)
calved from Chasm 1 on 2023-01-23 (British Antarctic Survey Press Office, 2023; U. S. National Ice Center, 2023). BIS has
thus exhibited a cycle of rifting and calving, accompanied by dynamic changes related to the degree of buttressing provided
90 by MIR (Gudmundsson et al., 2017; De Rydt et al., 2019). A further calving event may occur as a result of the propagation of
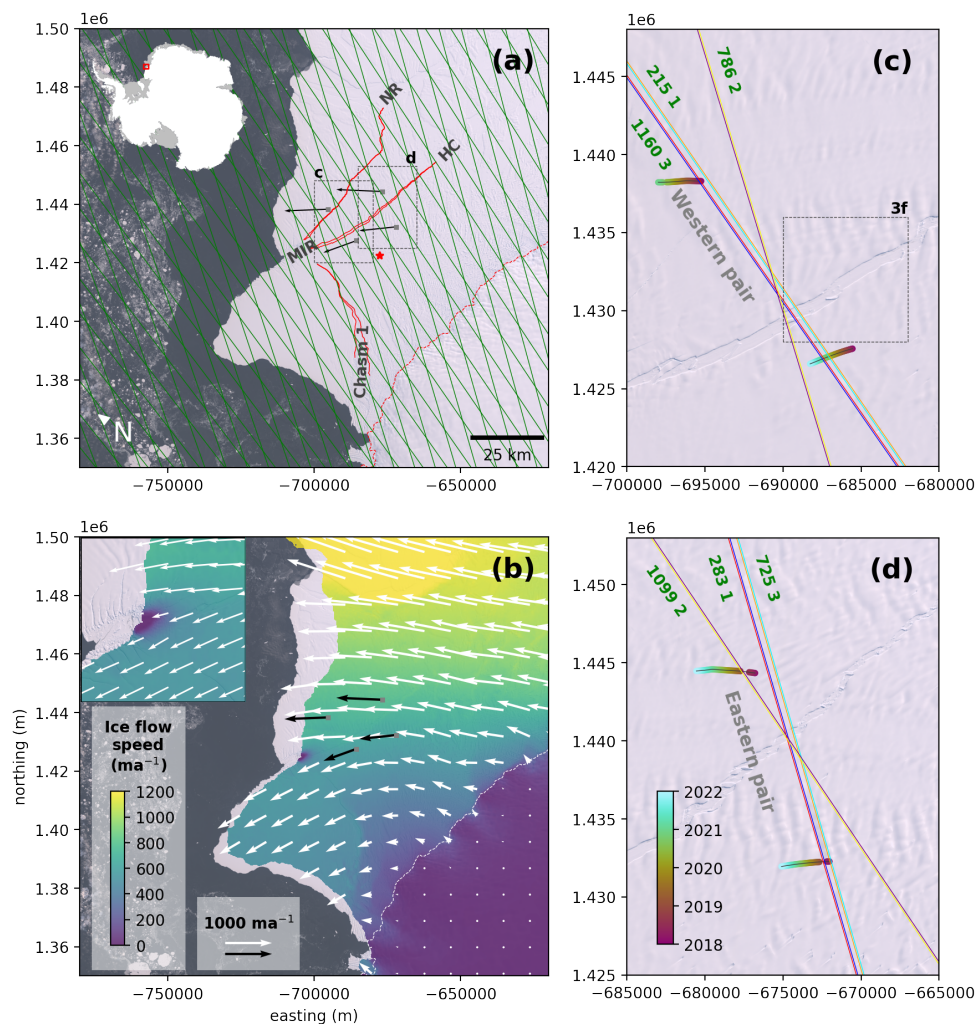
Figure 1. Key glaciological features of Brunt Ice Shelf, instrument locations and ICESat-2 ground tracks. (**a**) Landsat-8 image from 2020-02-20 showing Chasm 1, Halloween Crack (HC) and North Rift (NR) in solid red lines; McDonald Ice Rumples (MIR); the grounding zone (Bindschadler et al., 2011) with a dashed red line; Halley VI station with red star; GNSS receivers with gray squares, flow direction and magnitude with arrows; extent of c and d with dashed boxes; ICESat-2 reference ground track (RGT) with green lines. Inset shows the location of Brunt Ice Shelf in East Antarctica (Data from the SCAR Antarctic Digital Database, accessed 2023). (**b**) Surface flow speed field (Gardner et al., 2018, 2020). Note the impact on the flow field of the pinning point at McDonald Ice Rumples (enlarged in inset). (**c**) Section of the ice shelf near the western end of HC, showing the location of the six beams (three pairs) of ICESat-2 passes along RGT 215, RGT 1160 and RGT 786. The dashed box shows the extent of Fig. 3f. (**d**) Section of the ice shelf near the eastern end of HC, showing ICESat-2 passes along RGT 283, RGT 725 and RGT 1099. Beam colors in c and d correspond to graphs in Figs. 4, 5 and 6. Colored points show the movement of the GNSS receivers through the deployment. Projection is Antarctic Polar Stereographic (EPSG: 3031).

HC. This will determine the immediate future of BIS, dependent on the level of contact maintained with MIR following the calving, and the response of the remaining ice shelf to potential unpinning (Hodgson et al., 2019; De Rydt et al., 2019).

## 3   Data and Methods

3.1   ICESat-2 Data and Rift Catalog

95   ICESat-2 is a laser altimetry satellite with an orbital inclination of 92° (allowing data collection to 88° S and full coverage of Antarctic ice shelves), and orbital repeat cycle of 91 days. The platform carries the ATLAS instrument, star trackers and an inertial measurement unit for pointing determination, and GPS receivers for positioning (Neumann et al., 2019). ATLAS is a photon counting laser altimeter designed to overcome the limitations of ICESat (Abdalati et al., 2010; Markus et al., 2017). It splits the transmitted 532 nm laser pulses into 6 beams (3 pairs), increasing spatial coverage and allowing calculation of across

100   track slope. One beam pair is at satellite nadir, the other pairs are 3.3 km to each side (Markus et al., 2017). Each beam pair consists of a strong beam and weak beam (with one quarter the energy) separated by 90 m. The platform pointing is maintained such that one beam in each pair is either side of a 'Reference Ground Track', requiring pointing precision better than 45 m (Markus et al., 2017).

Telemetered data include platform positioning, pointing, and individual photon time of flight (ATL02), from which the three

105   dimensional reflection point of individual photons can be calculated (latitude, longitude, height above ellipsoid). The ATL03 product is a point cloud of individual classified signal and background photon detections (Neumann et al., 2019). The land ice elevation product (ATL06) takes 40 m along-track segments of ATL03 (spaced 20 m apart) and fits a surface to signal photons, iteratively rejecting background photons. Each segment is assigned the elevation of the surface at the segment center (Smith et al., 2019). ATL06 greatly reduces data volume whilst maintaining sufficient detail for rift detection and measurement (Wang

110   et al., 2021, Fig. 1c).

ICESat-2 has been used previously to study crevassing, rifting and calving (Li et al., 2021; Walker et al., 2021; Wang et al., 2021; Becker et al., 2021). Of particular relevance, Wang et al. (2021) automated fracture detection in ICESat-2 ATL06 data by iteratively identifying low points and simulating filling them with water, until no further depressions could be found, then building a hierarchical structure linking depressions nested across multiple scales, and working top-down to identify individual

115   fractures which satisfy specified criteria.

The cataloging of rifts is a two step process: firstly identifying potential rifts, and secondly measuring various characteristics such as width (Fig. 3), ice mélange thickness, seaward-landward offset (Walker and Gardner, 2019), and rift flank topography (Walker et al., 2021; Fricker et al., 2005a). Before embarking on this process, we first subsetted ATL06 data to BIS using the BedMachine Antarctica floating ice mask (Morlighem, 2020; Morlighem et al., 2020). Each beam was then filtered by discard-

120   ing any ~4 km section with >20 % of measurements flagged as low quality and discarding unrealistic elevations (>100 m). Any beams with >3 % of gaps between elevation measurements exceeding 25 m were also discarded.

Potential rifts were identified using a 10 km running mean to create a smoothed ice shelf surface, any elevations below 50 % of this were identified as potential rifts (Fig. 3a). For each potential rift, an expanded search area was defined, centered on
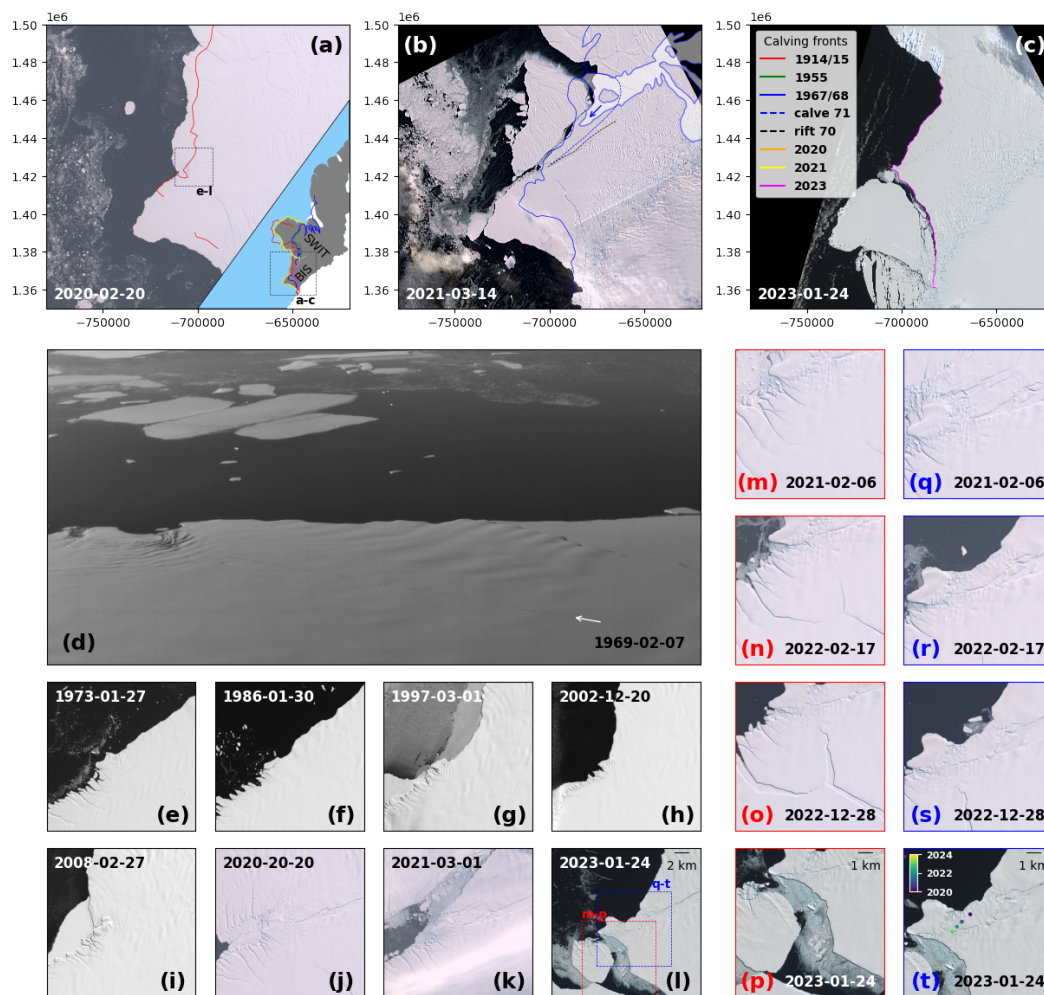
Figure 2. Calving front position of BIS and SWIT since 1914, showing cyclic rifting and calving east of MIR. (**a**) The 2020 front (Landsat-8 image) compared to the 1914/15 (red) position from HMS *Endurance* (digitized from Thomas, 1973). Inset shows the calving front positions of the wider area between 1914/15 and 2023. (**b**) Iceberg calving (A-74) from NR and HC position in February 2021 (Copernicus Sentinel-2 data [2021]), compared to 1967/68 front (blue), rift (dashed black) and area which calved in 1971 (dashed blue (all digitized from Thomas, 1973)). White area shows parts of the 1967/68 shelf composed of sea ice. Blue arrow shows a potential partial rift. (**c**) Iceberg calving (A-81) from Chasm 1 on 2023-01-23 (Copernicus Sentinel-2 data [2023]). (**d**) Part of an aerial photograph from 1969 looking north towards MIR, showing the rift which calved in 1971. (**e–l**) Landsat-1 to Landsat-9 and Sentinel-2 imagery of BIS in the vicinity of MIR between 1973 and 2023, showing the re-advance east of MIR and subsequent calving. Dashed red and blue boxes in l show the extent of m–p and q–t respectively. (**m–p**) Propagation and opening of Chasm 1 and a smaller frontal rift leading to the calving of iceberg A-81. (**q–t**) The accumulation of damage upstream of MIR to the nascent iceberg between HC and the ice front following calving from NR. Points in t show the path of the western tip of HC between 2020 and 2023.
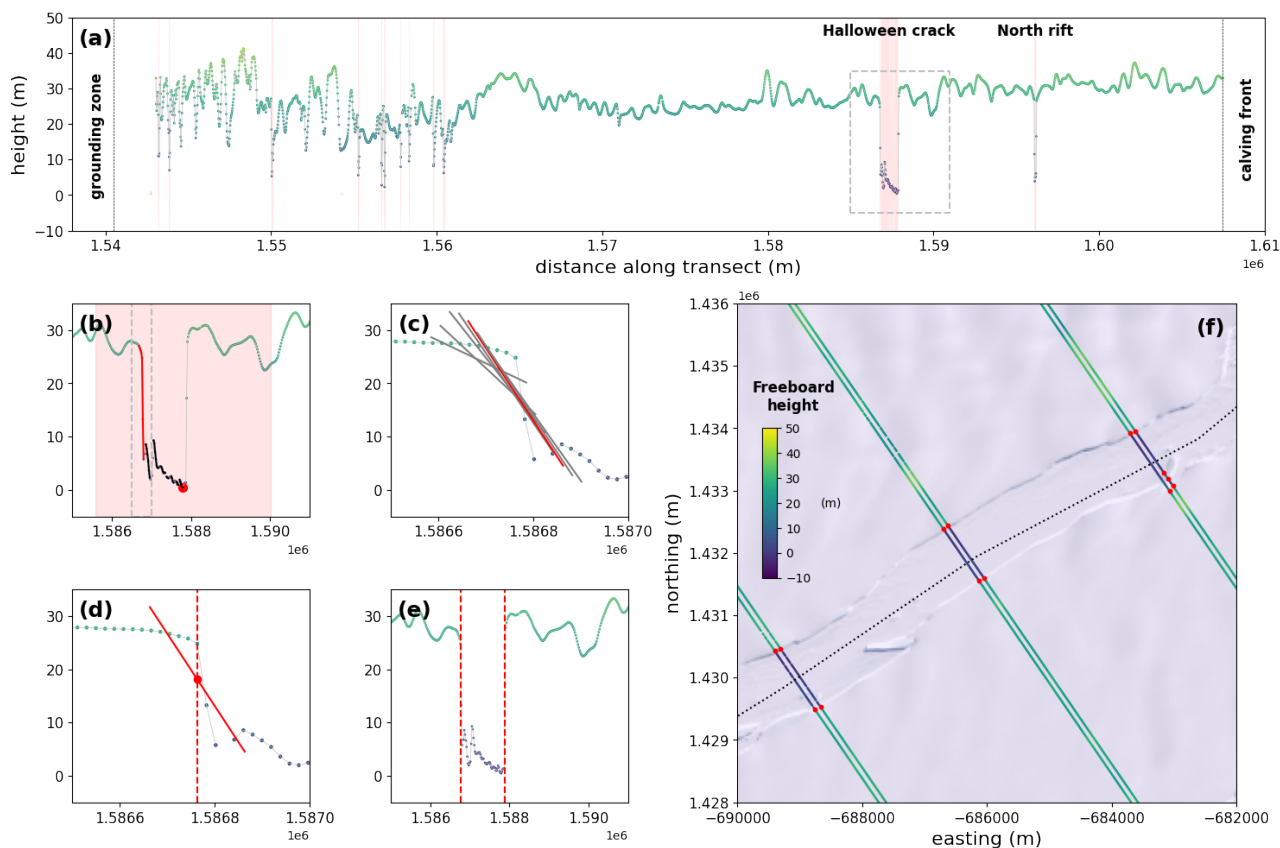
Figure 3. Example rift detection and measurement along RGT 215 1L on 2021-01-07. (**a**) ICESat-2 ATL06 transect with potential rifts shown as light red bars. Dashed box around HC shows the extent of b and e. (**b**) Expanded search area (light red box) centered on the lowest point in the rift (red circle). The mostly likely rift wall (red) is selected from the possibilities (black). Dashed box shows the extent of c and d. (**c**) The steepest section of the rift wall (red line) is selected from measurements of slope along 200 m sections (gray lines). (**d**) The location of the rift wall (dashed red line) is defined as the average location of points in steepest section (red line). (**e**) The process is repeated for the opposite rift wall. (**f**) Rift detections (red circles) along the six beams of RGT 215 overlaid on a Landsat-8 image from the same day. The dashed line traces the rift axis, which is used to estimate rift widths from oblique measurements. The same elevation colorbar is used throughout.

the lowest point (Fig. 3b). Working outwards in both directions from this point, upward sloping regions were identified. The probable rift walls were identified as the first upward sloping region to exceed 50 % of rift depth, or the largest upward sloping region within the search region if none exceed 50 %.

We then measured rift width using the following workflow: the slope was calculated for ~200 m sections centered on each ATL06 measurement along the probable rift wall (Fig. 3c), with the average location of ATL06 points making up the steepest slope taken to be representative of wall location (Fig. 3d). The apparent rift width is the distance between the two rift walls

130 (Fig. 3e); this was converted to actual width according to the angular offset between the ground track and a plane perpendicular to the large-scale rift axis (Fig. 3f). Where the rift is bisected by a block (e.g. Figs. S7a–f, S9d–i), both the "wall-to-wall width" and "opening width" were cataloged (Fig. S4). As validation of the workflow, ICESat-2-derived widths were compared with measurements from digitized optical satellite imagery and the separation of GNSS receivers.

3.2 Satellite Imagery

We examined Landsat-8, Landsat-9 and MAXAR WorldView-1-3 optical satellite imagery of HC during cloud-free days in Austral summer. Forty nine Landsat-8 and Landsat-9 images covered the entirety of HC (Table S5), 20 WorldView-1-3 images covered western HC (Table S1), and 18 covered eastern HC (Table S2). Relevant RGTs were overlain on the satellite imagery in QGIS, and rift width measured using the "measure" tool. Opening widths were calculated and apparent widths converted to
140 actual widths in the same way as the ICESat-2 measurements. Digitization error was assumed to be two pixels for each wall, meaning a greater error where the rift is bisected by a block.

We also used Landsat-1, Landsat-5, Landsat-7, Landsat-8, Landsat-9 and Sentinel-2 satellite imagery, combined with historical aerial photographs, and digitized calving front and rift positions from Thomas (1973) to provide context for recent rifting events and to investigate the long-term behavior of BIS, updating the record of Anderson et al. (2014).

145

3.3 Global Navigation Satellite System

The British Antarctic Survey maintain a network of Leica GS-10 GNSS receivers both landward and seaward of HC to monitor its growth (Figs. 1, S2 and S3). These record at 30 second intervals for two hours each day between 14:00 and 16:00 UTC. Daily averaged positions are calculated using precise point positioning. Receivers tt05 and hh00 (hereafter the "western pair")
150 form a baseline approximately perpendicular to the rift axis and aligned with RGT 215 1LR and RGT 1160 3LR. RGT 786 2LR measures the same area of the rift, but is oblique to the rift-perpendicular plane (Fig. 1c). Likewise, the baseline between receivers tt04 and ss00 (the "eastern pair") is approximately aligned with RGT 283 1LR and RGT 725 3LR, and oblique to RGT 1099 2LR (Fig. 1d), with all somewhat oblique to the rift-perpendicular plane. This configuration provides an excellent dataset for validation of the workflow for measurement of apparent rift width and conversion to actual width.
155 Polar Stereographic coordinates representative of the positions of each GNSS receiver on 15th of each month were calculated by fitting lines of best fit to any month with >15 daily positions. Time series of monthly GNSS separation were then calculated for each GNSS pair, and the angle of the monthly baseline used to calculate the rift-perpendicular component. Finally, an estimate for the rate of rift-perpendicular ice divergence was calculated by extracting the velocity components at the mean locations of the GNSS receivers from a pre-HC initiation (2015) velocity map (Gardner et al., 2018, 2020), and subtracted
160 from the rift-perpendicular separation time series. This has the effect of removing residual horizontal strain within the intact ice shelf adjacent to the rift. This then provides a better approximation of the rift opening rate that would be measured by

GNSS receivers placed close to the rift walls.

3.4 Ice Flow Model

165   We compare HC opening rates from the three datasets to opening rates calculated using modeled ice flow fields for three periods centred on the calving event from NR; labeled "pre-calving", "calving" and "post-calving" inverse models (Table S8). We also examine the response of wider ice shelf flow field to the calving event. We use the Python-based finite element glacier and ice sheet flow modeling library *icepack*, and the *Firedrake* partial differential equation solver package on which it is built (Shapero et al., 2021; Rathgeber et al., 2016). *icepack* includes solvers for common glaciological modeling problems, including

170   the shallow shelf approximation used here ("IceShelf" model class). We produce modeled velocity and fluidity fields using an inverse model which takes as inputs an initial-guess velocity field and a smoothed ice shelf thickness map. We also use these output velocity and fluidity fields as inputs to additional model runs to investigate the relative importance of geometry, velocity and fluidity changes.

  We used the co-registration and offset tracking functions of the SeNtinel Applications Platform (SNAP) to produce velocity

175   fields from 12-day repeat Sentinel-1 SAR image pairs, then applied a 15–by–15 pixel averaging filter to suppress noise. The thickness map was produced using ICESat-2 SlideRule (Swinski et al., 2022) data and smoothed using *icepack* to ensure sensible estimation of driving stress. The model domains were bound by the grounding line, MIR, calving fronts east and west of MIR, and a divide between BIS and SWIT defined by the extent of the observed velocity fields. We define the extent of HC and other smaller fractures in the vicinity of MIR (including the narrow, $\sim$13 km beginning of NR in the "pre-calving" model),

180   but not Chasm 1 (which consists of multiple fractures and a large area of damaged ice and mélange), meaning it is modeled as an area of low fluidity. Ice flows into the domain across the grounding line, the grounding line of MIR, and the BIS/SWIT divide. The inverse model is then used to estimate the fluidity coefficient A in Glen's flow law (Glen, 1955):

$$\dot{\epsilon}_{ij} = A\tau_E^{n-1}\tau_{ij} \tag{1}$$

where $n = 3$, $\dot{\epsilon}_{ij}$ and τ{ij} are the strain rate and deviatoric stress tensors, and $\tau_E = \sqrt{\tau_{ij}\tau_{ij}/2}$ is the effective deviatoric stress.

185   During inversion, we iteratively alter the fluidity field until it produces a velocity field that matches the input within a given tolerance (Shapero et al., 2021). The rate of rift opening is calculated as the difference in the rift perpendicular components of velocity extracted from locations within the modeled velocity fields along the baselines between the two GNSS pairs, and 100 m from the rifts walls.

4 Results

4.1 Historical Behavior of Brunt Ice Shelf

We used Landsat and Sentinel-2 imagery spanning half a century, and digitized maps from Thomas (1973) to examine the long-term rifting and calving behavior and resultant ice front positions of BIS and SWIT, building on the record of Anderson et al. (2014). The three oldest ice front positions (all from Thomas (1973)) are from 1914/15 (red line in Fig. 2a and inset; from Shackleton's HMS *Endurance* expedition), 1955 (green line in Fig. 2 inset; from Argentine icebreaker *General San Martín*), and 1967/68 (blue line in Fig. 2b and inset; combined ship and field data). We supplement these with ice front positions from 2020, 2021 and 2023 (orange, yellow and magenta lines respectively in Fig. 2 inset; from Landsat-8 and Sentinel-2 imagery), book-ending the calving of a $\sim$1270 km^2 iceberg from NR in February 2021, and a $\sim$1550 km^2 iceberg from Chasm 1 in January 2023. We discuss changes in three areas: SWIT, BIS east of MIR (area of HC and NR), and BIS west of MIR (area of Chasm 1).

The SWIT ice front was similarly advanced in 1914/15 and 2020/21, and $\sim$70 km landward in 1955 and 1967/68 (Fig. 2 inset). One or more large calving events from SWIT must have occurred between 1914/15 and 1955, and with the 2020/21 ice front close to the 1914/15 position, another may be expected in the coming decades. Between SWIT and MIR the 1914/15 BIS ice front is not as advanced as the 2020 ice front (Fig. 2a) and in the vicinity of MIR is more comparable to the ice front in $\sim$2000 (e.g. Fig. 2g–h). The 1967/68 and 2021 ice fronts are largely the same, barring an area to the east where a small area of the shelf was partially detached along a short fracture (blue arrow in Fig. 2b). There is a gap in the 1955 ice front in this area, but Anderson et al. (2014) present a 1958 ice front and suggest no large calving events occurred between 1958 and 1967/68. In 1968 a rift formed in largely the same location as HC (white arrow in Fig. 2d and black dashed line in b, note HC visible in the satellite imagery). This calved in 1971 (Thomas, 1973), resulting in the most retreated ice front position observed (blue dashed line in Fig. 2b). Calving from HC in the near future would result in a comparably retreated ice front position. To the west of MIR the 1914/15 ice front was more advanced than the 1967/68 ice front, evincing a calving event sometime during this interval (Fig. 2a inset). The 2020/21 ice front was considerably more advanced than either of the previous observations, and the reactivation of Chasm 1 around 2012 (De Rydt et al., 2018, 2019) suggested calving was imminent. Chasm 1 and a smaller rift initiating from the damaged ice front immediately downstream of MIR propagated and widened through the early 2020s until a $\sim$1550 km^2 iceberg (A-81) calved on 2023-01-23 (Fig. 2c, m–p).

4.2 Rift Measurement Algorithm Performance and Halloween Crack Behavior

4.2.1 Rift Measurement Algorithm Performance

Our rift measurement algorithm successfully produced 375 measurements of HC width along 17 RGTs (Table 1, Fig. S2). Five additional measurements were underestimated by $\sim$100 m as a result of a block dividing the rift and all ATL06 measurements in one part being flagged as low quality. This compares to 440 times HC could be identified manually in the ICESat-2 data

Table 1. The number of times HC could be manually identified in ICESat-2 ATL06 data spanning 2018-10-14 to 2021-07-15, compared to the number of times it was found and measured by the rift detection and measurement algorithm. The five errors were rift width underestimations caused by semi-detached ice blocks bisecting the rift and all the points within one part being flagged as low quality.

| RGT	Manual	ICESat-2	Percent	error
McDonald Ice Rumples				
276	2	1	50 %	0
1289	6	5	83 %	0
718	12	12	100 %	0
344	27	24	89 %	0
1160	**28**	**26**	**93** %	**0**
786	**58**	**49**	**84** %	**0**
215	**54**	**51**	**94** %	**0**
1228	40	36	90 %	0
657	33	30	91 %	1
283	**27**	**26**	**96** %	**0**
1099	**23**	**23**	**100** %	**0**
725	**26**	**23**	**88** %	**1**
154	30	26	87 %	1
1167	24	19	79 %	0
596	34	21	62 %	2
222	12	7	58 %	0
1038	4	1	25 %	0
Stancomb-Wills Ice Tongue				
Total	440	380	86 %	5

(86 %). The percentage is higher at the center of HC, where the rift is widest, and decreases towards the rift tips (Table 1). The 60 times HC was not recorded were times the segment of the beam was not processed due to poor data quality, or elevation measurements along one or both rift walls did not satisfy a number of confidence criteria. Rift wall identifications were discarded if they contained fewer than three elevation measurements, if more than 25 % of measurements were flagged as low quality, or if the measurement density was low (defined as the average along-track separation exceeding 50 m).

Five of the six reference ground tracks used for validation exceed the average measurement success percentage (RGT 215, RGT 1160, RGT 283, RGT 725 and RGT 1099 (Table 1), with RGT 786 2 % below average. However, this includes beam pairs which are not used, and the corresponding measurement success percentages for the individual beam pairs were: RGT 215 1LR 94 %; RGT 1160 3LR 100 %; RGT 786 2LR 83 %; RGT 283 1LR 100 %; RGT 725 3LR 73 %; RGT 1099 2LR 100 %. Removing width measurements effected by satellite pointing errors early in the ICESat-2 mission leaves between 3 and 8 width
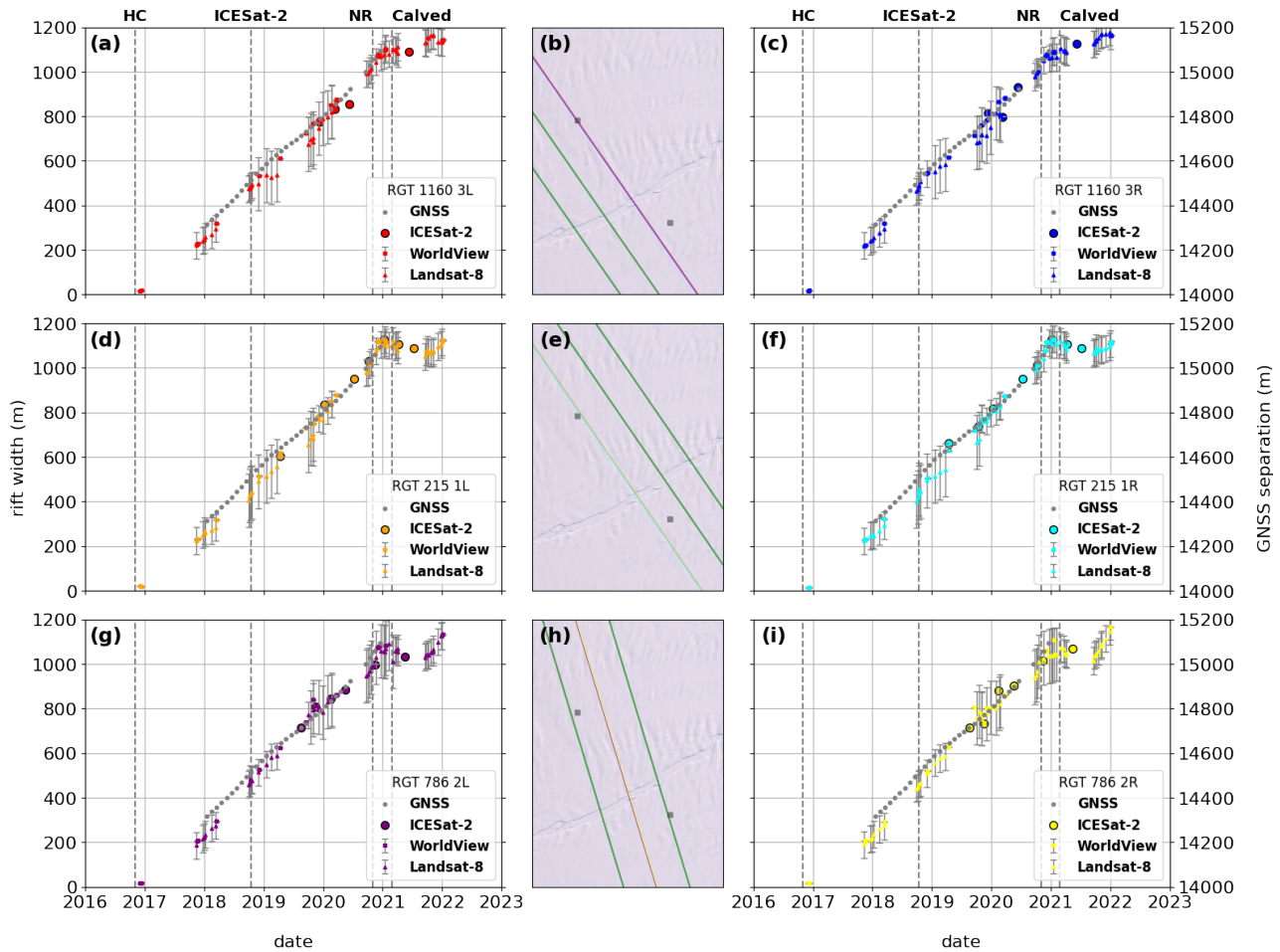
Figure 4. Time series of HC actual widths from the application of the rift measurement algorithm to ICESat-2 ATL06 data (circles), digitization on WorldView-1-3 (squares) and Landsat-8 (triangles) satellite imagery, and the component of the separation of the western pair of GNSS receivers (Fig. 1c) perpendicular to the local rift axis and corrected for divergence (gray circles) for (**a–c**) RGT 1160 3LR, (**d–f**) RGT 215 1LR and (**g–i**) RGT 786 2LR. Colors correspond to the beam colors in Fig. 1c. Error bars on WorldView-1-3 and Landsat-8 points denote a two pixel margin for digitization error, and therefore are twice as large where an ice block bisects the rift. Dashed lines denote the timing of the first observation of Halloween Crack (**HC**), the launch of ICESat-2 (**ICESat-2**), the observation of North Rift propagation (**NR**), and the calving of an iceberg from North Rift (**Calved**). ICESat-2 derived widths from passes with large satellite pointing errors were excluded from this analysis.

measurements per beam (mean: 4.6, median: 4). This allows us to validate HC width estimates from ICESat-2 with independent estimates from satellite imagery and field-based measurements on a beam-by-beam basis (Figs. 4 and 5), but to ensure a sufficient number of points for robust estimation of rift opening rate it was necessary to combine all width measurements for

235 each GNSS pair (Fig. 6).
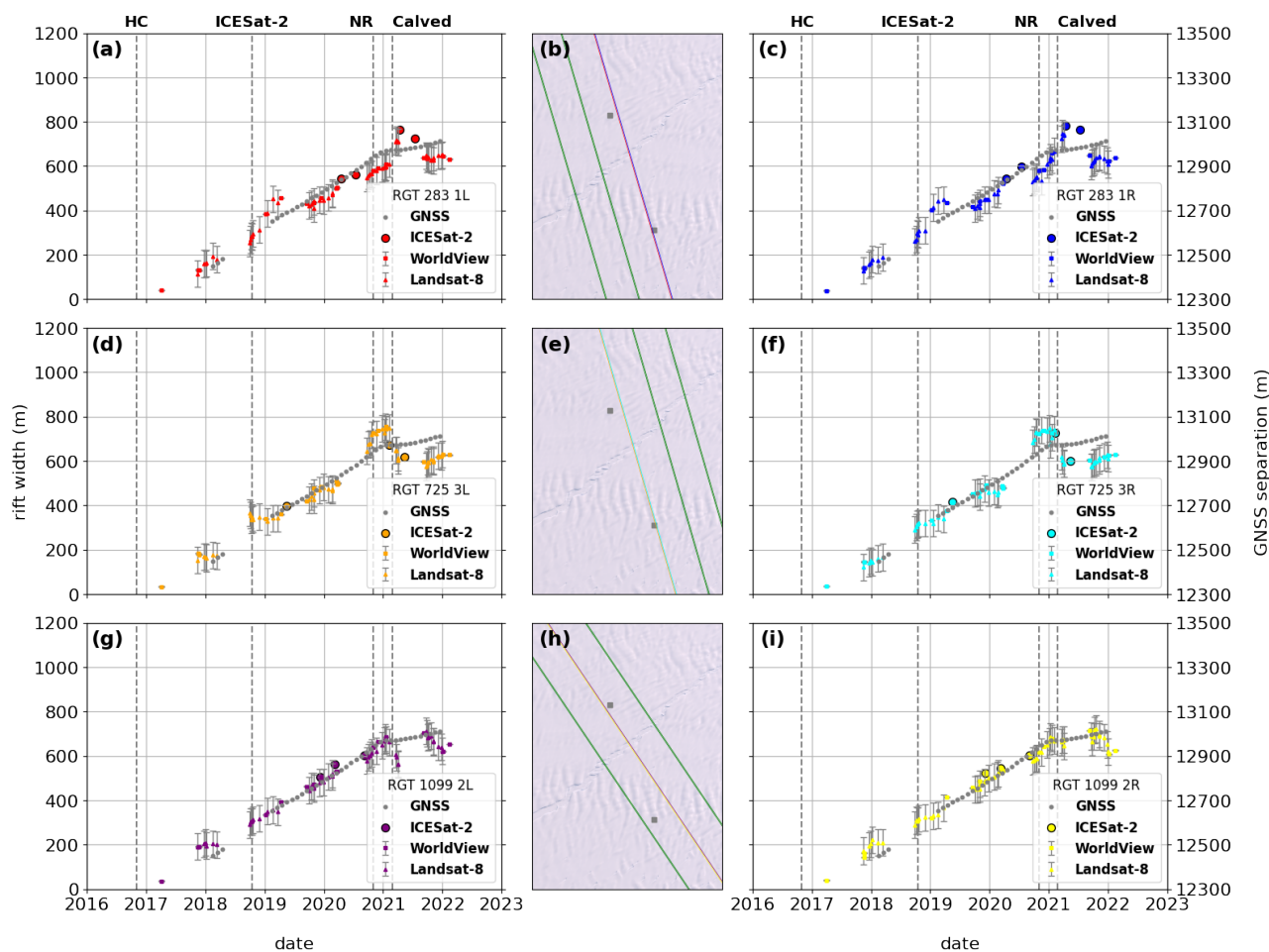
Figure 5. As Fig. 4 for (**a–c**) RGT 283 1LR, (**d–f**) RGT 725 3LR and (**g–i**) RGT 1099 2LR. Colors correspond to the beam colors in Fig. 1d.

4.2.2 Comparison with Satellite Imagery and GNSS Observations

We compare the western GNSS receivers to RGT 215 1LR, RGT 1060 3LR, and RGT 786 2LR. The western GNSS receivers move apart at an almost constant rate, with no apparent seasonal variability. (We present detailed rift opening rate calculations in the next subsection.) Rift initiation ('HC') precedes the first GNSS measurements by around a year, but the trend suggests a

240   similar rate of opening through this first year. The seaward GNSS receiver (hh00, Fig. S2) was located seaward of NR which began propagating in late-2020 (Fig. 1a), and was removed just prior to calving in February 2021. As a result, the HC width time series calculated from the separation of the western GNSS pair ends at the end of 2020. Throughout the period between the initiation of HC and calving from NR, estimates of HC width from ICESat-2 and digitized satellite imagery were generally consistent with the GNSS estimates, with some variability around the trend line. Measurements from ICESat-2 and digitized

245   satellite imagery continue after the calving from NR, and show that rift opening stagnated temporarily in the period immedi-

ately following the calving (Fig. 4d and f).

We compare the eastern GNSS receivers with RGT 283 1LR, RGT 725 3LR, and RGT 1099 2LR. The seaward GNSS of the eastern pair was located between HC and NR (Fig. 1a), and therefore the GNSS record continues after the calving from NR (Fig. 5), clearly showing the considerable reduction in HC opening rate following NR calving, then a gradual increase

250   remaining below the pre-calving rate for the remainder of the study period. Close examination of the eastern GNSS pair record suggests this reduction in HC opening rate occurred between the timing of NR propagation and eventual calving (We use 2021-01-01 as the threshold between before and after calving opening rates in Fig. 6 and Table 2). The individual HC width estimates from ICESat-2 and digitized satellite imagery again generally follow the trend line, although individual ICESat-2 measurements and groups of satellite imagery-derived measurements exhibit larger offsets from the width reconstructed from

255   GNSS receiver separation (e.g. along RGT 283 1LR immediately following calving from the NR).

4.2.3   Rift Opening Rates

Given that the three RGTs used in each comparison with GNSS pairs measure almost the same portion of HC (Fig. 1c and d), it is possible to combine all widths from ICESat-2 and all widths from satellite imagery to estimate opening rates for rift areas

260   between the western and eastern GNSS pairs using the three independent datasets (Fig. 6, Table 2). We calculate opening rates for the periods before and after calving from NR. The pre-calving rates calculated from ICESat-2 and satellite imagery agreed to within $\sim$25 $\mathrm{m\,a^{-1}}$ (246.3 $\mathrm{m\,a^{-1}}$; 270.6 $\mathrm{m\,a^{-1}}$) for western HC, and to within $\sim$15 $\mathrm{m\,a^{-1}}$ (144.0 $\mathrm{m\,a^{-1}}$; 158.0 $\mathrm{m\,a^{-1}}$) for eastern HC. The rates were also consistent with the estimated rift opening rate from the GNSS separations within $\sim$30 $\mathrm{m\,a^{-1}}$ (254.5 $\mathrm{m\,a^{-1}}$ for western pair, 176.9 $\mathrm{m\,a^{-1}}$ for eastern pair). The northernmost GNSS of the western pair was removed prior to

265   calving, leaving only the eastern pair. This measured a post-calving opening rate of 46.1 $\mathrm{m\,a^{-1}}$, with an acceleration in opening rate (from 23.3 $\mathrm{m\,a^{-1}}$ to 66.9 $\mathrm{m\,a^{-1}}$) apparent if the after calving record is split at 2021-06-30. This is the only reliable post calving opening rate, those from ICESat-2 and satellite imagery vary between -84.9 $\mathrm{m\,a^{-1}}$ and 32.5 $\mathrm{m\,a^{-1}}$, though with low R^2 values and in the case of ICESat-2 low confidence in the calculated opening rates evinced by the wide 95 % confidence intervals resulting from short time series with high spread, and few ICESat-2 measurements. Taken together, the three datasets

270   are evidence of a reduction in the rate of HC opening following calving from NR, including possible short-lived stagnation.

4.2.4   Comparison with Modeled Ice Flow

HC opening rates were calculated as the difference between the rift perpendicular components of modeled ice flow at the intersection of the rift and eastern and western GNSS receiver pair baselines (Fig. 7a–i). Modeled opening rates show good agreement with observations during the "pre-calving" period. During this time, modeled rates on HC were 257.0 $\mathrm{m\,a^{-1}}$ for

275   the western pair and 193.1 $\mathrm{m\,a^{-1}}$ for the eastern pair (Fig. 7a, d–e). This is consistent with the western pair observations, and $\sim$20–50 $\mathrm{m\,a^{-1}}$ greater than the eastern pair observations, though the pattern of greater opening in the west is correctly modeled. Following calving, the modeled opening rates drop to 53.6 $\mathrm{m\,a^{-1}}$ and 36.4 $\mathrm{m\,a^{-1}}$ respectively (Fig. 7b, f–g). The (low confidence) stagnation or even gradual closing suggested by the ICESat-2 measurements particularly between the western pair
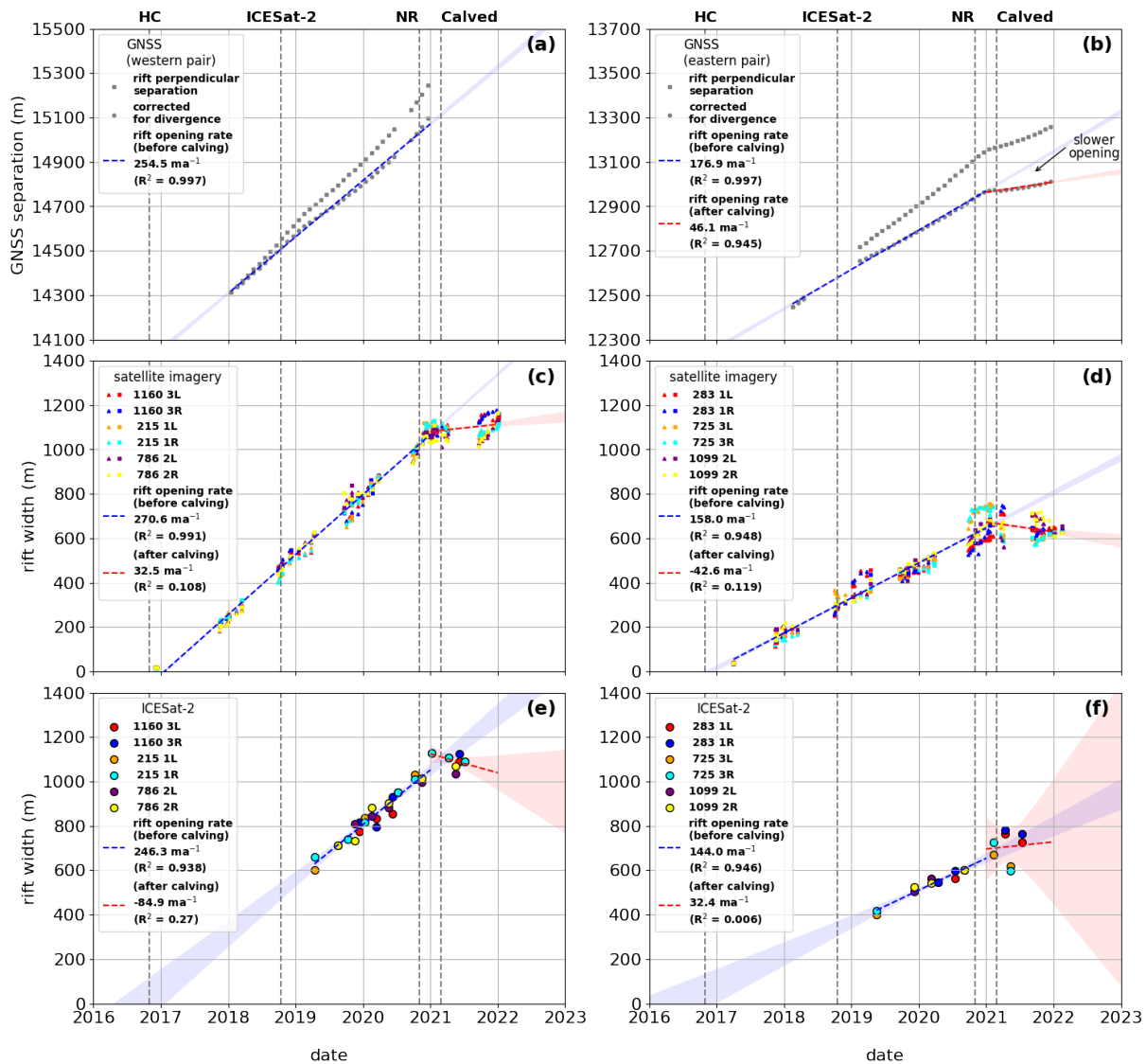
Figure 6. Independent estimates from the three datasets of the rates of HC opening in the vicinity of the GNSS pairs before and after calving from NR. (**a**, **b**) Time series of the component of the separation of the pairs of GNSS receivers perpendicular to the local rift axis (gray squares) and corrected for divergence (gray circles). (**c**) Combined time series of HC width from WorldView-1-3 (squares) and Landsat-8 (triangles) for RGT 215 1LR, RGT 1160 3LR, and RGT 786 2LR. (**d**) As c for RGT 283 1LR, RGT 725 3LR and RGT 1099 2LR. (**e**) Combined time series of HC width from ICESat-2 (circles) for RGT 215 1LR, RGT 1160 3LR, and RGT 786 2LR. (**f**) as e for RGT 283 1LR, RGT 725 3LR and RGT 1099 2LR. Point colors in c and e correspond to Figs. 1c and 4, point colors in d and f correspond to Figs. 1d and 5. Dashed lines show rates of HC opening before (blue) and after (red) 2021-01-01 using a linear fit. Light blue and red regions show corresponding 95 % confidence intervals.

(Fig. 4) is not replicated, though the modeled rates are far lower than those from the "pre-calving" and "post-calving" models,
and are consistent with the gradual opening calculated from the eastern GNSS pair. The "post-calving" rates of $136.5\,\mathrm{m\,a^{-1}}$
and $87.6\,\mathrm{m\,a^{-1}}$ (Fig. 7c, h–i) are consistent in pattern with the renewed but more gradual than before calving opening observed
by the eastern GNSS pair, though are larger in magnitude (Figs. 5 and 6b). The inverse models therefore replicate the general
pattern of opening rates, but may underestimate the degree of transient stagnation following calving from NR.

We carried out a set of modeling experiments with the goal of determining the cause of the deceleration of opening rates
along HC. First we carried out a set of experiments in which we only changed the ice geometry, simulating the calving of
iceberg A-74 (using the "calving" and "post-calving" domains). These model runs (Diagnostic$_2$ to Diagnostic$_5$ in Table S9)
used the inferred fluidity field and domain boundary velocity field from the "pre-calving" inverse model. These models do not
replicate the observed reduction in HC opening rates. The ice geometry is therefore not solely responsible for the change in
opening rates. Next we carried out a set of experiments in which we changed the ice geometry and domain boundary velocity
fields (using the output velocity fields from the "calving" and "post-calving" inverse models), keeping the inferred fluidity field
fixed (Diagnostic$_6$ to Diagnostic$_9$ in Table S9). These models captured the decrease in HC opening rates during the "calving"
period ($66.7\,\mathrm{m\,a^{-1}}$ and $55.8\,\mathrm{m\,a^{-1}}$ for west and east respectively compared to $53.6\,\mathrm{m\,a^{-1}}$ and $36.4\,\mathrm{m\,a^{-1}}$ from the inverse
model). They also capture, but overestimate, the increase in HC opening rate during the "post-calving" period ($181.5\,\mathrm{m\,a^{-1}}$
and $154.8\,\mathrm{m\,a^{-1}}$ for west and east respectively compared to $136.5\,\mathrm{m\,a^{-1}}$ and $87.6\,\mathrm{m\,a^{-1}}$ from the inverse model).

Across the wider ice shelf, the inverse models show ice flow speeds increased (compare black "pre-calving" arrow length to
colored "calving" and "post-calving" arrow length in Fig. 7j, k), as happened following calving in 1971 (Gudmundsson et al.,
2017). The colored arrows denote the angular redirection of ice flow following calving. To the west of BIS the ice flow seaward
of Chasm 1 rotated clockwise as the nascent iceberg (A-81) which would calve on 2023-01-23 pivoted about the remaining
connection to the remainder of the shelf (Fig. 2m–p; (Cheng et al., 2021b)). Across the east and the nascent iceberg between
HC and the new calving front the flow direction rotated anti-clockwise. The ice flow direction in the central portion of the
shelf remained largely unchanged. The change in fluidity parameter (dashed areas in Fig. 7p) shows the advection of Chasm 1
(decreasing upstream and increasing downstream, as well as some errors in the feature tracked velocity field in this area) and
an increase in the grounding zone.

5 Discussion

5.1 Validation of Rift Measurement Algorithm

Optical remote sensing and the GNSS receivers installed to monitor the growth of HC provide two independent datasets with
which to validate the individual HC width measurements and rate of HC opening measurements from ICESat-2. Measurements
of HC width between the western pair from the three datasets show excellent agreement (Fig. 4). In the vicinity of the western
pair, the rift is largely straight-sided, with only occasional small-scale topography leading to minor offsets between the three
datasets. Larger offsets are apparent for the eastern GNSS pair (Fig. 5), though the individual detections of apparent width
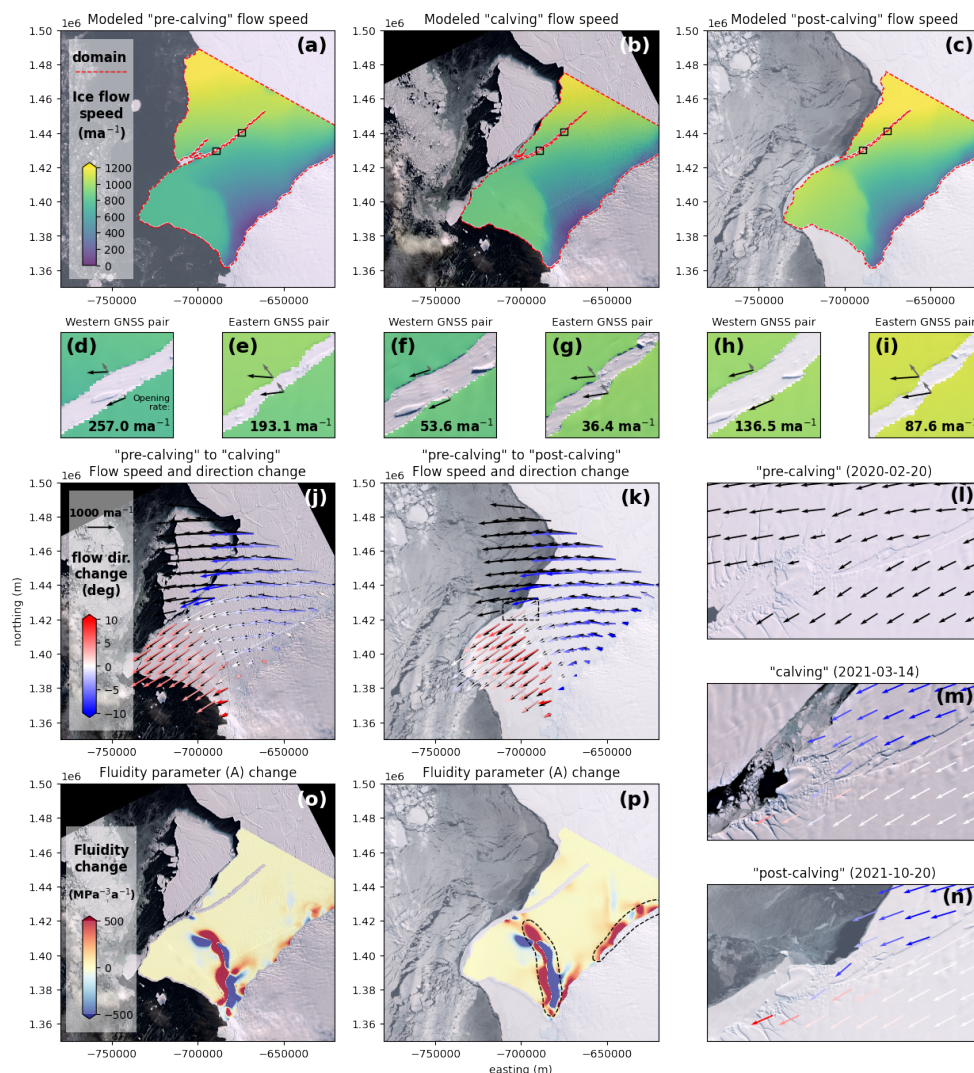
Figure 7. Results of *icepack* inverse modeling of HC opening rates for "pre-calving", "calving" and "post-calving" periods. (**a–c**) Modeled ice flow speed within the model domain (dashed red line). (**d–i**) Modeled ice velocity (black arrow) and rift perpendicular component (gray arrow) either side of HC from which opening rate is calculated for the western and eastern GNSS pairs. Solid black boxes in a–c show the locations of d–i. (**j, k**) Modeled ice flow direction and magnitude change. Colored arrows show the angular change in flow direction for the "calving" and "post-calving" periods compared to the "pre-calving" period (black arrows). Dashed black box in k shows the location of l–n. (**l–n**) Modeled ice velocity and degree of contact between BIS and MIR during the three periods. (**o, p**) Change in the modeled fluidity parameter (A) between between the "calving" and "pre-calving" periods (o) and "post-calving" and "pre-calving" periods (p). Dashed regions in p outline areas with large changes in modeled fluidity.

The Cryosphere
Discussions

Table 2. HC opening rates for the areas between the western and eastern GNSS pairs from GNSS separation measurements, Landsat-8/WorldView-1-3 (Satellite) width measurements, ICESat-2 width measurements, and ice flow modeling. For ICESat-2 and satellite measurements, results from three RGTs are combined (RGT 215 1LR, RGT 1160 3LR, and RGT 786 2LR for the western GNSS pair, RGT 283 1LR, RGT 725 3LR, and RGT 1099 2LR for the eastern GNSS pair). Opening rates for before and after 2021-01-01 (between NR propagation and calving) are shown for GNSS, Satellite and ICESat-2 measurements. Modeled opening rates are calculated for the "pre-calving", "calving" and "post-calving" periods as the difference of the rift perpendicular components of ice flow, as shown in Fig. 7. Descriptions and observed opening rates with high (low) confidence are shown in bold (regular). The seaward GNSS receiver of the western pair was removed prior to calving from NR in February 2021.

Dataset	Description/Opening rate $(\mathrm{m\,a^{-1}})$					
	Western			Eastern		
	pre-calving	calving	post-calving	pre-calving	calving	post-calving
GNSS	**rapid opening 254.5**	GNSS removed		**rapid opening 176.9**		**gradual opening 46.1**[a]
Satellite	**rapid opening 270.6**	gradual opening 32.5[b]		**rapid opening 158.0**		gradual closing -42.6[b]
ICESat-2	**rapid opening 246.3**	gradual closing -84.9[b]		**rapid opening 144.0**		gradual opening 32.4[b]
Model (253 K)	257.0	53.6	136.5	193.1	36.4	87.6

[a] Accelerating from 23.3 m a^{-1} between 2021-01-01 and 2021-06-30 to 66.9 m a^{-1} between 2021-07-01 and 2021-12-31. [b] Low confidence opening rate ($R^2 = 0.006$–0.27) as a result of short records and the effect of small-scale rift wall undulations and meanders (Fig. S6).

appear robust (Figs. S13 to S15). The offsets are the result of small-scale meanders in HC formed as it propagated between meteoric ice blocks and deviated from the large-scale rift axis (De Rydt et al., 2018; King et al., 2018), leading to increases in measured width (Fig. S6).

315 Combining the three RGT beam pairs for each GNSS pair allows the calculation of the rate of rift opening from the three datasets (Fig. 6 and Table 2). Prior to calving from NR there was good agreement ($\sim$25 m a^{-1}) between rates of HC opening from ICESat-2, from digitization of optical satellite imagery, and from pairs of GNSS receivers separated by >10 km, despite varying temporal ranges, rift wall topography, and uncertainty in the divergence correction to the GNSS measurements. This

provides validation for the rift measurement workflow presented here. The close agreement also indicates that rift widening, at

320 least in the case of HC, is dominated by rift wall divergence rather than calving along the rift walls. Large-scale calving occurs primarily along fractures originating from the initial stages of rift formation, while small-scale collapses of material from the rift walls are very localized. The differences between the rates of rift wall separation (ICESat-2 and satellite imagery) and rates reconstructed from GNSS separation are likely explained by uncertainty in the ice flow divergence calculation caused by any lateral offset of the GNSS receivers from the rift-perpendicular axis in the vicinity of the ICESat-2 ground tracks. It is also pos-

325 sible that differences arise as a result of the differing reference frames; the ICESat-2 RGTs along which ICESat-2 and Satellite imagery width were measured are fixed in space (Eulerian reference frame), whereas the rift and the GNSS receivers move with ice flow (Lagrangian reference frame). The rift parallel component of ice flow near the GNSS pairs ($\sim$700–1000 $\mathrm{m\,a^{-1}}$) is much smaller than the length of HC ($\sim$50 km), so the resulting uncertainty in rift opening rate due to differing reference frames is <10 $\mathrm{m\,a^{-1}}$ (Fig. S15), within the assumed divergence correction uncertainty.

330 During the period of NR propagation and calving the rate of HC opening reduced or even stagnated (with some observations suggesting rift closing, though with high uncertainty in the case of ICESat-2 between the western GNSS pair (Fig. 6e) and the potential for meandering rift wall topography to mask the opening rate signal in the case of the satellite imagery between the eastern GNSS pair (Fig. 6d)). The most complete record, from the eastern GNSS pair suggests this reduced opening/stagnation was transient, with the rate of HC opening gradually increasing through to the end of the record (approximately one year after

335 calving). Whilst not influenced by variable rift wall topography, there is uncertainty associated with the divergence correction. However, it is clear that a significant change in HC behavior occurred during the period in which NR was propagating and eventually calving. From a validation point of view, the spread in opening rate measurements after calving caution against over-interpretation of temporally short records or those with opening rates close to 0 $\mathrm{m\,a^{-1}}$, where uncertainties resulting from rift wall topography, rift advection, and random measurement errors could be greater than the signal. For example, in Fig. 6c-d

340 the large number of satellite measurements leads to small uncertainties in the opening rates (narrow 95 % confidence intervals), but the west and east show contrasting behavior. We attribute this to the effect of meandering rift wall topography in the east. In Fig. 6e-f the small number of ICESat-2 measurements, high spread, and short record results in low confidence opening rates (broad 95 % confidence intervals). Fig. 6f is the only record for which a continuation or increase of rapid opening following NR calving is within the 95 % confidence interval. Taken together, the three datasets are evidence of reduction in the rate of

345 HC opening, including the possibility of transient stagnation.

5.2 Behaviour of Halloween Crack and Brunt Ice Shelf from observations and modeling

The observations and ice flow modeling allow us to observe the response of floating ice and a rift to a calving event. Many studies have looked at grounded ice after ice shelf calving, but few if any have looked at the details of ice shelf flow and

350 fracture in the immediate post-calving period. Between the initiation of HC and propagation of NR, the rate of opening was essentially constant on an inter-annual timescale, with no substantial seasonal modulation (Figs. 4 and 5) resulting from any variation in ice mélange mechanical strength or other potential external forcing mechanisms. This suggests that the rate of HC

opening was controlled primarily by glaciological stresses. In November 2020 a further rift (NR) propagated seaward of HC, calving a $\sim$1270 km^2 iceberg in February 2021. The widening of HC slowed (possibly to the point of stagnation) in the months

355 immediately following calving, before returning to opening at a reduced rate (Figs. 4, 5 and 6). Given the lack of sensitivity of HC to seasonal forcing prior to calving, the close timing of calving and reduced opening, and the mid-summer timing of the calving event, it is extremely unlikely that increased ice mélange mechanical strength contributed to the reduced opening rate. We also do not observe large changes in ice thickness which could have significantly altered the force balance at the calving front (Figs. S18–S21).

360 Prior to calving (and since $\sim$2000 (Fig. 2f, g)), ice flowed "head-on" into MIR, resulting in ice rumples and damage in the form of fractures visible up- and down-glacier. Ice bifurcated, flowing to the north and south of MIR. This divergence of flow vectors (Fig. 7l), and the tensile stresses generated upstream of the zone of compression, likely combine to drive initiation and widening of HC and NR. Following calving, all ice flow is to the south of MIR. Ice flow across much of the east of the shelf and nascent iceberg between HC and the new calving front rotated anti-clockwise (Fig. 7j, k), resulting in a reduction

365 in the rift perpendicular component of ice flow seaward of HC, thereby reducing the opening rate (compare Fig. 7d and f). The additional model runs (Table S9) elucidate on the mechanisms responsible for the pattern of changes in HC opening rate. The model runs in which we only changed the ice geometry did not replicate the observations. The model runs in which we changed the ice geometry and domain boundary velocity fields but kept the inferred fluidity field constant qualitatively match the observations, exhibiting a decrease to very low opening rates in the "calving" period and a resumption of opening in the

370 "post-calving" period, though remaining lower than the opening rates in the "pre-calving" period. However, quantitatively the agreement between the inverse and additional model runs for the "calving" period are much closer than the "post-calving" period. Taken together, this suggests that the primary driver is the change in geometry and resultant change in large-scale ice flow, though changes in fluidity, including the increase in fluidity in the grounding zone (likely indicative of fracture growth; dashed region in Fig. 7p) make a secondary contribution.

375 The resumption of HC opening at a slower rate following the period of stagnation shown by the eastern GNSS pair (Fig. 5) and "post-calving" model (Fig. 7c, h, i) may suggest stagnation was a transient response to calving, but is more likely due to deformation and the accumulation of damage on the nascent iceberg $\sim$3 km upstream of MIR, as the western tip of HC moves clockwise around the south of MIR (Fig. 2q–t). In spite of the transient pause in HC opening, with the eastern tip approaching an area of fragmented shelf ice with large areas of sea ice, and damage accumulating immediately upstream of MIR, calving

380 from HC in the coming years cannot be ruled out.

5.3 Historical Behavior of Brunt Ice Shelf

Our analysis of Landsat imagery and digitized maps allows us to investigate the calving cycle at BIS (section 4.1). It is possible that the BIS ice front east of MIR advanced after 1914/15, reaching a position similar to that in the 2010s, with a significant area of ice north of MIR. One or more calving events, possibly an event similar to the 2021 calving, must have occurred

385 sometime between 1914/15 and 1955. The position of the 1914/15 front in the vicinity of MIR being similar to that in $\sim$2000 (Fig. 2g–h; $\sim$20 years before the 2021 calving event) likely favoring the mid to latter part of this interval. An alternative inter-

pretation could be repeating smaller calving events between 1914/15 and 1955 from similarly placed rifts. It is notable that the area between the 1967/68 and 1971 fronts is similar to the area between the 2021 front/NR and HC (Fig. 2b). A hypothesized repeating pattern of dual rift formation and twin calving events, with the smaller event (1971 calving from the 1968 rift and

390   future calving from HC) delayed relative to the larger event (hypothesized 1914/15–1955 calving and 2021 calving from NR) is therefore consistent with the available data. However, the timing of rift initiation would be different, with the 1968 rift forming decades after the hypothesized calving between 1914/15 and 1955, whereas HC and NR formed close together in time and in the opposite order (HC in 2016 and NR in 2020). Figure 2d does show a more significant area of ice to the north of MIR than in 2021 following calving from NR (Fig. 2k), possibly suggesting considerable advance since the previous calving event.

395   Regardless of the sequence of events, the importance MIR and local ice geometry to rift initiation is apparent.

To the west of MIR, the degree of contact between MIR and BIS was not immediately reduced as a consequence of the calving in January 2023. This amounts to ∼2350 m, of which ∼1500 m is with ice between HC and the new ice front following calving from NR, and ∼850 m is with the remainder of the shelf. Damage is accumulating within the nascent HC iceberg ∼3 km upstream of MIR (Fig. 2q–t), allowing the resumption of opening of the bulk of the rift. The degree of contact maintained

400   between MIR and the remainder of the shelf following any future calving from HC will be crucial in determining the response of BIS to calving (Hodgson et al., 2019).

Focusing on MIR (Fig. 2d–l), we show that BIS maintained contact following the 1971 calving event, with visible pressure ridges and damage to the ice downstream demonstrating that it was providing some buttressing to the ice shelf throughout. However, ice flow is largely parallel to the 1973, 1986 and 1997 calving fronts in the vicinity of MIR (Figs. 2e–g and 1b inset),

405   so in the three decades following the 1971 calving event MIR was a source of lateral drag. By ∼2000 (Fig. 2 g–h) the ice front east of MIR had re-advanced sufficiently to flow "head-on" into MIR. This results in divergent and ultimately bifurcating ice flow, and generates tensile stresses upstream to the east of MIR which are ultimately responsible for the initiation and opening of HC and NR rifts (and previously the 1968 rift). Gudmundsson et al. (2017) observed a gradual decrease of BIS flow velocities (which had doubled following the 1971 calving) after ∼2000 as a result of the increased flow resistance. These

410   observations suggest that the flow velocity could more than double should calving from HC result in a loss of contact between BIS and MIR. This would be unprecedented in the observational record, and could have implications of the stability of BIS (Hodgson et al., 2019).

6   Conclusions

415   We have presented a method for the measurement of ice shelf rift width and opening rate from ICESat-2 ATL06 data. For each rift detection, the algorithm searches for the most likely landward and seaward walls, and calculates the slope for overlapping ∼200 m sections, defining the rift wall location as the mean of the points in the steepest section. Where the rift is divided in two by a semi-detached block or iceberg, both the "opening width" and "wall-to-wall width" are calculated. Finally, the apparent rift width is converted to an estimate of actual width using the angular offset between the ICESat-2 track and a plane

420 perpendicular to the large-scale rift axis.

The rift width measurement algorithm and resulting estimates of opening rate were validated using Halloween Crack on Brunt Ice Shelf as a case study. HC width was digitized on optical Landsat-8 and WorldView-1-3 satellite imagery, and a time-series of ice flow divergence-corrected, rift-perpendicular separation distance calculated from the locations of two pairs of GNSS receivers. Between the western GNSS pair, where HC is straight-sided, measurement success was 84–94 % (Table 1) and the

425 three datasets exhibited good consistency in individual width measurements and rates of rift opening prior to calving from NR (Figs. 4 and 6). Between the eastern pair (88–100 %), there were some deviations in individual rift width measurements caused by small-scale meandering of the rift (Fig. 5), but equivalent consistency between rates of rift opening calculated from the three datasets. The consistency of rift measurements prior to calving from NR from remote sensing datasets and reconstructed using GNSS measurements, along with visual inspection of the measurements (Figs. S7–S14), gives confidence in the performance

430 of the algorithm. It also demonstrates the growth of HC is largely due to wall divergence, with calving from the walls being a minor contributor.

Following the 2021 calving from NR, HC opening rate dropped significantly, possibly to the point of stagnation, before returning to opening at a reduced rate. In this period the difference between the three opening rate datasets was greater due to the proportionally larger effect of uncertainties, cautioning against the over-interpretation of short records with low magnitude

435 signals. We attribute the changes in behavior primarily to changes in the geometry of the ice shelf in the vicinity of MIR, and the resulting reorganization of the ice shelf flow field. Prior to calving BIS flowed "head-on" into MIR, with some ice passing to the north of the pinning point. This generated tensile stresses and highly divergent ice flow upglacier (Fig. 7l), sufficient to initiate ice fracture and maintain the high opening rates observed in the early part of the record. Calving from NR in February 2021 removed ice flowing to the north of MIR, reducing flow resistance and resulting in a reorganization of ice flow across

440 the east of the shelf and the nascent iceberg between HC and the new calving front (Fig. 7j, k, m, n). The anti-clockwise rotation of flow reduced the difference in rift perpendicular components of ice flow (e.g. Fig. 7d, f, h), leading to the observed stagnation/lower opening rate of HC. The flow of the ice shelf appears to be accelerating in response to the reduction in flow resistance at MIR, as previously occurred following calving in 1971 (Gudmundsson et al., 2017). The calving of a $\sim$1550 km^2 iceberg (A-81) from Chasm 1 in January 2023 did not immediately result in a further reduction in the level of contact between

445 BIS and MIR (Fig. 2c, m–p), though the accumulation of damage on the nascent HC iceberg $\sim$3 km upstream of MIR and the resumption of HC opening are signs that a further calving event may occur (Fig. 2q–t). We used satellite imagery and historical observations to study the calving cycle at BIS (Fig. 2), demonstrating the remarkable similarity in the locations of HC and a rift that calved in 1971, and NR/post-calving ice front and the 1967/68 ice front (Thomas, 1973). So, whilst calving from a HC-like rift is not unprecedented, the western tip of the 1971 rift had not propagated clockwise around MIR to the degree HC

450 has. The future behavior of BIS will depend on the development of HC and the level of contact maintained between BIS and MIR following a calving event. A complete loss of contact with MIR would be unprecedented in the observational record. This could lead to ice flow speeds more than doubling, and have implications for the stability of BIS (Hodgson et al., 2019). More widely, ice rises and ice rumples are prevalent across Antarctica (Matsuoka et al., 2015) suggesting the potential for further instances of changes in the dynamics of floating ice and neighboring rifts (as well as the widely studied changes in grounding

455 zone flux) in response to calving events.

We have shown that ICESat-2 can supplement optical satellite imagery for the spaceborne monitoring of ice shelf rifts, with the advantage of year-round observations only limited by the presence of cloud cover. The algorithm presented here, when combined with a validated rift detection algorithm (that distinguishes between rifts and crevasses) is readily scalable to the entire Antarctic Ice Sheet. It is hoped that making available a catalog of rift characteristics such as width, ice mélange thickness, and

460 rift topography through the duration of the lifetime of ICESat-2 will facilitate further study into ice shelf fracture and calving processes, and thus contribute to better constraint of the likely future mass balance of the Antarctic Ice Sheet.

Code and data availability. Scripts used to detect and measure rifts as part of the "Antarctic Rift Catalog" project are available at https://doi.org/10.5281/zenodo.7839138 (Morris et al., 2023). These scripts will be updated as the project progresses. *icepack* is an open source

465 ice flow modeling package available at https://github.com/icepack/icepack. *icepack* model runs detailed here are available at https://doi.org/10.5281/zenodo.7796399 (Morris and Lipovsky, 2023).

Appendix A

Author contributions. AM led the research and the writing of the manuscript. BPL and CCW designed the 'Antarctic Rift Catalog' Project and supervised the research. BPL contributed to code development. OJM processed GNSS data from Brunt Ice Shelf. All authors contributed

470 to the writing of the manuscript.

Competing interests. The authors declare no competing interests

Table A1. List of Acronyms

Abbreviation	Definition
ATLAS	Advanced Topographic Laser Altimeter System
ATL02	ICESat-2 photon time of flight, spacecraft positioning and pointing data
ATL03	ICESat-2 Global Geolocated Photon data
ATL06	ICESat-2 Land ice elevation product
BIS	Brunt Ice Shelf
GNSS	Global Navigation Satellite System
HC	Halloween crack
ICESat	Ice, Cloud, and Land Elevation Satellite
ICESat-2	Ice, Cloud, and Land Elevation Satellite 2
MIR	McDonald Ice Rumples
NASA	National Aeronautics and Space Administration
NR	North Rift
RGT	ICESat-2 Reference Ground Track
RGT 215 1LR	Reference Ground Track 215 beam pair 1
RGT 1160 3LR	Reference Ground Track 1160 beam pair 3
RGT 786 2LR	Reference Ground Track 786 beam pair 2
RGT 283 1LR	Reference Ground Track 283 beam pair 1
RGT 725 3LR	Reference Ground Track 725 beam pair 3
RGT 1099 2LR	Reference Ground Track 1099 beam pair 2
SNAP	SeNtinel Applications Platform
SWIT	Stancomb-Wills Ice Tongue

deficiencies (Crameri et al., 2020). The supplementary material contains the following citations: Andersen and Knudsen (2009); De Rydt et al. (2018); Gardner et al. (2018, 2020); King et al. (2018); Morlighem (2020); Pavlis et al. (2012); Swinski et al. (2022).

References

485   Abdalati, W., Zwally, H. J., Bindschadler, R., Csathó, B., Farrell, S. L., Fricker, H. A., Harding, D., Kwok, R., Lefsky, M., Markus, T., Marshak, A., Neumann, T., Palm, S., Schutz, B., Smith, B., Spinhirne, J., and Webb, C.: The ICESat-2 Laser Altimetry Mission, Proceedings of the IEEE, 98, 735–751, https://doi.org/10.1109/JPROC.2009.2034765, 2010.

Andersen, O. B. and Knudsen, P.: The DNSC08 mean sea surface and mean dynamic topography, Journal of Geophysical Research, p. C11, https://doi.org/10.1029/2008JC005179, 2009.

490   Anderson, R., Jones, D. H., and Gudmundsson, G. H.: Halley Research Station, Antarctica: calving risks and monitoring strategies, Natural Hazards and Earth System Sciences, 14, 917–927, https://doi.org/10.5194/nhess-14-917-2014, 2014.

Aster, R. C., Lipovsky, B. P., Cole, H. M., Bromirski, P. D., Gerstoft, P., Nyblade, A., Wiens, D. A., and Stephen, R.: Swell-triggered seismicity at the near-front damage zone of the Ross Ice Shelf, Seismological Society of America, 92, 2768–2792, https://doi.org/10.1785/0220200478, 2021.

495   Banwell, A. F., Willis, I. C., Macdonald, G. J., Goodsell, B., Mayer, D. P., Powell, A., and MacAyeal, D. R.: Calving and rifting on the McMurdo Ice Shelf, Antarctica, Annals of Glaciology, 58, 78–87, https://doi.org/10.1017/aog.2017.12, 2017.

Bassis, J. N., Coleman, R., Fricker, H. A., and Minster, J. B.: Episodic propagation of a rift on the Amery Ice Shelf, East Antarctica, Geophysical Research Letters, 32, https://doi.org/10.1029/2004GL022048, 2005.

Bassis, J. N., Fricker, H. A., Coleman, R., Bock, Y., Behrens, J., Darnell, D., Okal, M., and Minster, J.-B.: Seismicity and deformation
500   associated with ice-shelf rift propagation, Journal of Glaciology, 53, 523–536, https://doi.org/10.3189/002214307784409207, 2007.

Bassis, J. N., Fricker, H. A., Coleman, R., and Minster, J.-B.: An investigation into the forces that drive ice-shelf rift propagation on the Amery Ice Shelf, East Antarctica, Journal of Glaciology, 54, 17–27, https://doi.org/10.3189/002214308784409116, 2008.

Becker, M. K., Howard, S. L., Fricker, H. A., Padman, L., Mosbeux, C., and Siegfried, M. R.: Buoyancy-Driven Flexure at the Front of Ross Ice Shelf, Antarctica, Observed With ICESat-2 Laser Altimetry, Geophysical Research Letters, 48, e2020GL091 207,
505   https://doi.org/10.1029/2020GL091207, 2021.

Benn, D. I., Warren, C. R., and Mottram, R. H.: Calving processes and the dynamics of calving glaciers, Earth-Science Reviews, 82, 143–179, https://doi.org/10.1016/j.earscirev.2007.02.002, 2007.

Bindschadler, R., Choi, H., Wichlacz, A., Bingham, R., Bohlander, J., Brunt, K., Corr, H., Drews, R., Fricker, H., Hall, M., Hindmarsh, R., Kohler, J., Padman, L., Rack, W., Rotschky, G., Urbini, S., Vornberger, P., and Young, N.: Getting around Antarctica: new high-
510   resolution mappings of the grounded and freely-floating boundaries of the Antarctic Ice Sheet created for the International Polar Year, The Cryosphere, 5, 569–588, https://doi.org/10.5194/tc-5-569-2011, 2011.

Borstad, C., McGrath, D., and Pope, A.: Fracture propagation and stability of ice shelves governed by ice shelf heterogeneity, Geophysical Research Letters, 44, 4186–4194, https://doi.org/10.1002/2017GL072648, 2017.

British Antarctic Survey Press Office: Brunt Ice Shelf in Antarctica calves, https://www.bas.ac.uk/media-post/
515   brunt-ice-shelf-in-antarctica-calves/, accessed: 2023-03-01, 2021.

British Antarctic Survey Press Office: Brunt Ice Shelf in Antarctica calves giant iceberg, https://www.bas.ac.uk/media-post/
brunt-ice-shelf-in-antarctica-calves-giant-iceberg/, accessed: 2023-03-01, 2023.

Bromirski, P. D. and Stephen, R. A.: Response of the Ross Ice Shelf, Antarctica, to ocean gravity-wave forcing, Annals of Glaciology, 53, 163–172, https://doi.org/10.3189/2012AoG60A058, 2012.

520 Bromirski, P. D., Sergienko, O. V., and MacAyeal, D. R.: Transoceanic infragravity waves impacting Antarctic ice shelves, Geophysical Research Letters, 37, https://doi.org/10.1029/2009GL041488, 2010.

Brunt, K. M., Okal, E. A., and MacAyeal, D. R.: Antarctic ice-shelf calving triggered by the Honshu (Japan) earthquake and tsunami, March 2011, Journal of Glaciology, 57, 785–788, https://doi.org/10.3189/002214311798043681, 2011.

Cathles IV, L. M., Okal, E. A., and MacAyeal, D. R.: Seismic observations of sea swell on the floating Ross Ice Shelf, Antarctica, Journal of
525 Geophysical Research: Earth Surface, 114, https://doi.org/10.1029/2007JF000934, 2009.

Cheng, Y., Xia, M., Qiao, G., Li, Y., Hai, G., and Lv, D.: Calving cycle of Ninnis Glacier over the last 60 years, International Journal of Applied Earth Observation and Geoinformation, 105, 102 612, https://doi.org/10.1016/j.jag.2021.102612, 2021a.

Cheng, Y., Xia, M., Qiao, G., Lv, D., Li, Y., and Hai, G.: Imminent calving accelerated by increased instability of the Brunt Ice Shelf, in response to climate warming, Earth and Planetary Science Letters, 572, 117 132, https://doi.org/10.1016/j.epsl.2021.117132, 2021b.

530 Christie, F. D. W., Benham, T. J., Batchelor, C. L., Rack, W., Montelli, A., and Dowdeswell, J. A.: Antarctic ice-shelf advance driven by anomalous atmospheric and sea-ice circulation, Nature Geoscience, 15, 356–362, https://doi.org/10.1038/s41561-022-00938-x, 2022.

Crameri, F., Shephard, G. E., and Heron, P. J.: The misuse of colour in science communication, Nature communications, 11, 5444, https://doi.org/10.1038/s41467-020-19160-7, 2020.

De Rydt, J., Gudmundsson, G. H., Nagler, T., Wuite, J., and King, E. C.: Recent rift formation and impact on the structural integrity of the
535 Brunt Ice Shelf, East Antarctica, The Cryosphere, 12, 505–520, https://doi.org/10.5194/tc-12-505-2018, 2018.

De Rydt, J., Gudmundsson, G. H., Nagler, T., and Wuite, J.: Calving cycle of the Brunt Ice Shelf, Antarctica, driven by changes in ice shelf geometry, The Cryosphere, 13, 2771–2787, https://doi.org/10.5194/tc-13-2771-2019, 2019.

Depoorter, M. A., Bamber, J. L., Griggs, J. A., Lenaerts, J. T. M., Ligtenberg, S. R., van den Broeke, M. R., and Moholdt, G.: Calving fluxes and basal melt rates of Antarctic ice shelves, Nature, 502, 89–92, https://doi.org/10.1038/nature12567, 2013.

540 Dupont, T. K. and Alley, R. B.: Assessment of the importance of ice-shelf buttressing to ice-sheet flow, Geophysical Research Letters, 32, https://doi.org/10.1029/2004GL022024, 2005.

Fox-Kemper, B., Hewitt, T. H., Xiao, C., Adalgeirsdóttir, G., Drijfhout, S. S., Edwards, T. L., Golledge, N. R., Hemer, M., Kopp, R. E., Krinner, G., Mix, A., Notz, D., Nowicki, S., Nurhati, I. S., Ruiz, L., Sallée, J.-B., Slangen, A. B. A., and Yu, Y.: Chapter 9: Ocean, Cryosphere and Sea Level Change, in: Climate Change 2021: The Physical Science Basis. Contribution of Working Group I to the Sixth
545 Assessment Report of the Intergovernmental Panel on Climate Change, edited by Masson-Delmotte, V., Zhai, P., Pirani, A., Connors, S. L., Péan, C., Berger, S., Caud, N., Chen, Y., Goldfarb, L., Gomis, M. I., Huang, M., Leitzell, K., Lonnoy, E., Matthews, J. B. R., Maycock, T. K., Waterfield, T., Yelekçi, O., Yu, R., and Zhou, B., pp. 1211–1362, Cambridge University Press, United Kingdom and New York, NY, USA, https://doi.org/10.1017/9781009157896.011, 2021.

Francis, D., Mattingly, K. S., Lhermitte, S., Temimi, M., and Heil, P.: Atmospheric extremes caused high oceanward sea surface slope trig-
550 gering the biggest calving event in more than 50 years at the Amery Ice Shelf, The Cryosphere, 15, 2147–2165, https://doi.org/10.5194/tc-15-2147-2021, 2021.

Francis, D., Fonseca, R., Mattingly, K. S., Marsh, O. J., Lhermitte, S., and Cherif, C.: Atmospheric triggers of the Brunt Ice Shelf calving in February 2021, Journal of Geophysical Research: Atmospheres, p. e2021JD036424, https://doi.org/10.1029/2021JD036424, 2022.

Fretwell, P., Pritchard, H. D., Vaughan, D. G., Bamber, J. L., Barrand, N. E., Bell, R., Bianchi, C., Bingham, R. G., Blankenship, D. D.,
555 Casassa, G., Catania, G., Callens, D., Conway, H., Cook, A. J., Corr, H. F. J., Damaske, D., Damm, V., Ferraccioli, F., Forsberg, R., Fujita, S., Gim, Y., Gogineni, P., Griggs, J. A., Hindmarsh, R. C. A., Holmlund, P., Holt, J. W., Jacobel, R. W., Jenkins, A., Jokat, W., Jordan, T., King, E. C., Kohler, J., Krabill, W., Riger-Kusk, M., Langley, K. A., Leitchenkov, G., Leuschen, C., Luyendyk, B. P., Matsuoka, K.,

Mouginot, J., Nitsche, F. O., Nogi, Y., Nost, O. A., Popov, S. V., Rignot, E., Rippin, D. M., Rivera, A., Roberts, J., Ross, N., Siegert, M. J., Smith, A. M., Steinhage, D., Studinger, M., Sun, B., Tinto, B. K., Welch, B. C., Wilson, D., Young, D. A., Xiangbin, C., and Zirizzotti,

560   A.: Bedmap2: improved ice bed, surface and thickness datasets for Antarctica, The Cryosphere, 7, 375–393, https://doi.org/10.5194/tc-7-375-2013, 2013.

Fricker, H. A., Young, N. W., Allison, I., and Coleman, R.: Iceberg calving from the Amery Ice Shelf, East Antarctica, Annals of Glaciology, 34, 241–246, https://doi.org/10.3189/172756402781817581, 2002.

Fricker, H. A., Bassis, J. N., Minster, B., and MacAyeal, D. R.: ICESat's new perspective on ice shelf rifts: The vertical dimension, Geophys-

565   ical Research Letters, 32, https://doi.org/10.1029/2005GL025070, 2005a.

Fricker, H. A., Young, N. W., Coleman, R., Bassis, J. N., and Minster, J.-B.: Multi-year monitoring of rift propagation on the Amery Ice Shelf, East Antarctica, Geophysical Research Letters, 32, https://doi.org/10.1029/2004GL021036, 2005b.

Fürst, J. J., Durand, G., Gillet-Chaulet, F., Tavard, L., Rankl, M., Braun, M., and Gagliardini, O.: The safety band of Antarctic ice shelves, Nature Climate Change, 6, 479–482, https://doi.org/10.1038/nclimate2912, 2016.

570   Gardner, A. S., Moholdt, G., Scambos, T., Fahnstock, M., Ligtenberg, S., van den Broeke, M., and Nilsson, J.: Increased West Antarctic and unchanged East Antarctic ice discharge over the last 7 years, The Cryosphere, 12, 521–547, https://doi.org/10.5194/tc-12-521-2018, 2018.

Gardner, A. S., Fahnstock, M., and Scambos, T.: ITS_LIVE Regional Glacier and Ice Sheet Surface Velocities, Data archived at National Snow and Ice Data Center, https://doi.org/10.5067/6II6VW8LLWJ7, 2020.

Gerrish, L., Fretwell, P., and Cooper, P.: Medium resolution vector polygons of the Antarctic coastline (7.6) [Data set]., UK Polar Data Cen-

575   tre, Natural Environment Research Council, UK Research & Innovation., https://doi.org/10.5285/b5eaca58-2fce-4a68-bea5-fbafd7c90fa2, 2022.

Giles, A. B.: The Mertz Glacier Tongue, East Antarctica. Changes in the past 100 years and its cyclic nature - Past, present and future, Remote Sensing of Environment, 191, 30–37, https://doi.org/10.1016/j.rse.2017.01.003, 2017.

Glen, J. W.: The creep of polycrystalline ice, Proceedings of the Royal Society of London. Series A. Mathematical and Physical Sciences,

580   228, 519–538, https://doi.org/10.1098/rspa.1955.0066, 1955.

Greene, C. A., Gardner, A. S., Schlegel, N.-J., and Fraser, A. D.: Antarctic calving loss rivals ice-shelf thinning, Nature, 609, 948–953, https://doi.org/10.1038/s41586-022-05037-w, 2022.

Gudmundsson, G. H., De Rydt, J., and Nagler, T.: Five decades of strong temporal variability in the flow of Brunt Ice Shelf, Antarctica, Journal of Glaciology, 63, 164–175, https://doi.org/10.1017/jog.2016.132, 2017.

585   Gudmundsson, G. H., Paolo, F. S., Adusumilli, S., and Fricker, H. A.: Instantaneous Antarctic Ice Sheet mass loss driven by thinning ice shelves, Geophysical Research Letters, 46, 13 903–13 909, https://doi.org/10.1029/2019GL085027, 2019.

Heeszel, D. S., Fricker, H. A., Bassis, J. N., O'Neel, S., and Walter, F.: Seismicity within a propagating ice shelf rift: The relationship between icequake locations and ice shelf structure, Journal of Geophysical Research: Earth Surface, 119, 731–744, https://doi.org/10.1002/2013JF002849, 2014.

590   Hodgson, D. A., Jordan, T. A., Rydt, J. D., Fretwell, P. T., Seddon, S. A., Becker, D., Hogan, K. A., Smith, A. M., and Vaughan, D. G.: Past and future dynamics of the Brunt Ice Shelf from seabed bathymetry and ice shelf geometry, The Cryosphere, 13, 545–556, https://doi.org/10.5194/tc-13-545-2019, 2019.

Hulbe, C. L., LeDoux, C., and Cruikshank, K.: Propagation of long fractures in the Ronne Ice Shelf, Antarctica, investigated using a numerical model of fracture propagation, Journal of Glaciology, 56, 459–472, https://doi.org/10.3189/002214310792447743, 2010.

595 Joughin, I. and MacAyeal, D. R.: Calving of large tabular icebergs from ice shelf rift systems, Geophysical Research Letters, 32, https://doi.org/10.1029/2004GL020978, 2005.

Joughin, I., Shapero, D., Smith, B., Dutrieux, P., and Barham, M.: Ice-shelf retreat drives recent Pine Island Glacier speedup, Science Advances, 7, eabg3080, https://doi.org/10.1126/sciadv.abg3080, 2021.

King, E. C., De Rydt, J., and Gudmundsson, G. H.: The internal structure of the Brunt Ice Shelf from ice-penetrating radar analysis and

600   implications for ice shelf fracture, The Cryosphere, 12, 3361–3372, https://doi.org/10.5194/tc-12-3361-2018, 2018.

Larour, E., Rignot, E., and Aubry, D.: Modelling of rift propagation on Ronne Ice Shelf, Antarctica, and sensitivity to climate change, Geophysical Research Letters, 31, https://doi.org/10.1029/2004GL020077, 2004.

Larour, E., Rignot, E., Poinelli, M., and Scheuchl, B.: Physical processes controlling the rifting of Larsen C Ice Shelf, Antarctica, prior to the calving of iceberg A68, Proceedings of the National Academy of Sciences, 118, https://doi.org/10.1073/pnas.2105080118, 2021.

605 Li, G., Guo, J., Pei, L., Zhang, S., Tang, X., and Yao, J.: Extraction and Analysis of the Three-Dimensional Features of Crevasses in the Amery Ice Shelf Based on ICESat-2 ATL06 Data, IEEE Journal of Selected Topics in Applied Earth Observations and Remote Sensing, 14, 5796–5806, https://doi.org/10.1109/JSTARS.2021.3085302, 2021.

Libert, L., Wuite, J., and Nagler, T.: Automatic delineation of cracks with Sentinel-1 interferometry for monitoring ice shelf damage and calving, The Cryosphere, 16, 1523–1542, https://doi.org/10.5194/tc-16-1523-2022, 2022.

610 Lipovsky, B. P.: Ice Shelf Rift Propagation and the Mechanics of Wave-Induced Fracture, Journal of Geophysical Research: Oceans, 123, 4014–4033, https://doi.org/10.1029/2017JC013664, 2018.

Lipovsky, B. P.: Ice shelf rift propagation: stability, three-dimensional effects, and the role of marginal weakening, The Cryosphere, 14, 1673–1683, https://doi.org/10.5194/tc-14-1673-2020, 2020.

MacAyeal, D. R., Rignot, E., and Hulbe, C. L.: Ice-shelf dynamics near the front of the Filchner-Ronne Ice Shelf, Antarctica, revealed by

615   SAR interferometry: model/interferogram comparison, Journal of Glaciology, 44, 419–428, https://doi.org/10.3189/S0022143000002744, 1998.

MacAyeal, D. R., Okal, E. A., Aster, R. C., Bassis, J. N., Brunt, K. M., Cathles, L. M., Drucker, R., Fricker, H. A., Kim, Y.-J., Martin, S., Okal, M. H., Sergienko, O. V., Sponsler, M. P., and Thom, J. E.: Transoceanic wave propagation links iceberg calving margins of Antarctica with storms in tropics and Northern Hemisphere, Geophysical Research Letters, 33, https://doi.org/10.1029/2006GL027235,

620   2006.

MacGregor, J. A., Catania, G. A., Markowski, M. S., and Andrews, A. G.: Widespread rifting and retreat of ice-shelf margins in the eastern Amundsen Sea Embayment between 1972 and 2011, Journal of Glaciology, 58, 458–466, https://doi.org/10.3189/2012JoG11J262, 2012.

Markus, T., Neumann, T., Martino, A., Abdalati, W., Brunt, K., Csathó, B., Farrell, S., Fricker, H., Gardner, A., Harding, D., Jasinski, M., Kwok, R., Magruder, L., Lubin, D., Luthcke, S., Morison, J., Nelson, R., Neuenschwander, A., Palm, S., Popescu, S., Shum, C., Schutz,

625   B. E., Smith, B., Yang, Y., and Zwally, J.: The Ice, Cloud, and Land Elevation Satellite-2 (ICESat-2): Science requirements, concept, and implementation, Remote Sensing of Environment, 190, 260–273, https://doi.org/10.1016/j.rse.2016.12.029, 2017.

Massom, R. A., Scambos, T. A., Bennetts, L. G., Reid, P., Squire, V. A., and Stammerjohn, S. E.: Antarctic ice shelf disintegration triggered by sea ice loss and ocean swell, Nature, 558, 383–389, https://doi.org/10.1038/s41586-018-0212-1, 2018.

Matsuoka, K., Hindmarsh, R. C., Moholdt, G., Bentley, M. J., Pritchard, H. D., Brown, J., Conway, H., Drews, R., Durand, G., Goldberg,

630   D., et al.: Antarctic ice rises and rumples: Their properties and significance for ice-sheet dynamics and evolution, Earth-Science Reviews, 150, 724–745, https://doi.org/10.1016/j.earscirev.2015.09.004, 2015.

Morlighem, M.: MEaSUREs BedMachine Antarctica, Version 2. [floating ice mask, firn air content], Boulder, Colorado USA. NASA National Snow and Ice Data Center Distributed Active Archive Center, https://doi.org/10.5067/E1QL9HFQ7A8M, date Accessed: 2021, 2020.

635   Morlighem, M., Rignot, E., Binder, T., Blankenship, D., Drews, R., Eagles, G., Eisen, O., Ferraccioli, F., Forsberg, R., Fretwell, P., Goel, V., Greenbaum, J. S., Gudmundsson, H., Guo, J., Helm, V., Hofstede, C., Howat, I., Humbert, A., Jokat, W., Karlsson, N. B., Lee, W. S., Matsuoka, K., Millan, R., Mouginot, J., Paden, J., Pattyn, F., Roberts, J., Rosier, S., Ruppel, A., Seroussi, H., Smith, E. C., Steinhage, D., Sun, B., van den Broeke, M. R., van Ommen, T. D., van Wessem, M., and Young, D. A.: Deep glacial troughs and stabilizing ridges unveiled beneath the margins of the Antarctic Ice Sheet, Nature Geoscience, 13, 132–137, https://doi.org/10.1038/s41561-019-0510-8,

640   2020.

Morris, A. and Lipovsky, B. P.: *icepack* modeling of Brunt Ice Shelf flow field and Halloween Crack opening rate for "pre-calving", "calving" and "post-calving" periods, Zenodo, https://doi.org/10.5281/zenodo.7796399, 2023.

Morris, A., Lipovsky, B. P., and Walker, C. C.: Antarctic Rift Catalog: Antarctic Rift Measurement Algoithm v1.0, Zenodo, https://doi.org/10.5281/zenodo.7839138, 2023.

645   Mouginot, J., Rignot, E., and Scheuchl, B.: Sustained increase in ice discharge from the Amundsen Sea Embayment, West Antarctica, from 1973 to 2013, Geophysical Research Letters, 41, 1576–1584, https://doi.org/10.1002/2013GL059069, 2014.

Neumann, T. A., Martino, A. J., Markus, T., Bae, S., Bock, M. R., Brenner, A. C., Brunt, K. M., Cavanaugh, J., Fernandes, S. T., Hancock, D. W., Harbeck, K., Lee, J., Kurtz, N. T., Luers, P. J., Luthcke, S. B., Magruder, L., Pennington, T. A., Ramos-Izquierdo, L., Rebold, T., Skoog, J., and Thomas, T. C.: The Ice, Cloud, and Land Elevation Satellite – 2 mission: A global geolocated photon product derived from

650   the Advanced Topographic Laser Altimeter System, Remote Sensing of Environment, 233, https://doi.org/10.1016/j.rse.2019.111325, 2019.

Olinger, S. D., Lipovsky, B. P., Wiens, D. A., Aster, R. C., Bromirski, P. D., Chen, Z., Gerstoft, P., Nyblade, A. A., and Stephen, R. A.: Tidal and thermal stresses drive seismicity along a major Ross Ice Shelf rift, Geophysical Research Letters, 46, 6644–6652, https://doi.org/10.1029/2019GL082842, 2019.

655   Olinger, S. D., Lipovsky, B. P., Denolle, M. A., and Crowell, B. W.: Tracking the Cracking: a Holistic Analysis of Rapid Ice Shelf Fracture Using Seismology, Geodesy, and Satellite Imagery on the Pine Island Glacier Ice Shelf, West Antarctica, Geophysical Research Letters, 49, e2021GL097 604, https://doi.org/10.1029/2021GL097604, 2022.

Paolo, F. S., Fricker, H. A., and Padman, L.: Volume loss from Antarctic ice shelves is accelerating, Science, 348, 327–331, https://doi.org/10.1126/science.aaa0940, 2015.

660   Pavlis, N. K., Holmes, S. A., Kenyon, S. C., and Factor, J. K.: The development and evaluation of the Earth Gravitational Model 2008 (EGM2008), Journal of Geophysical Research: Solid Earth, 117, https://doi.org/10.1029/2011JB008916, 2012.

Pritchard, H. D., Ligtenberg, S. R. M., Fricker, H. A., Vaughan, D. G., van den Broeke, M. R., and Padman, L.: Antarctic Ice-Sheet loss driven by basal melting of ice shelves, Nature, 484, 502–505, https://doi.org/10.1038/nature10968, 2012.

Rathgeber, F., Ham, D. A., Mitchell, L., Lange, M., Luporini, F., McRae, A. T. T., Bercea, G.-T., Markall, G. R., and Kelly, P. H. J.:

665   Firedrake: automating the finite element method by composing abstractions, ACM Transactions on Mathematical Software (TOMS), 43, 1–27, https://doi.org/10.1145/2998441, 2016.

Rignot, E. and MacAyeal, D. R.: Ice-shelf dynamics near the front of the Filchner—Ronne Ice Shelf, Antarctica, revealed by SAR interferometry, Journal of Glaciology, 44, 405–418, https://doi.org/10.3189/S0022143000002732, 1998.

The Cryosphere
Discussions

Rignot, E., Jacobs, S., Mouginot, J., and Scheuchl, B.: Ice-shelf melting around Antarctica, Science, 341, 266–270,
670   https://doi.org/10.1126/science.1235798, 2013.

Rott, H., Müller, F., Nagler, T., and Floricioiu, D.: The imbalance of glaciers after disintegration of Larsen-B Ice Shelf, Antarctic Peninsula,
        The Cryosphere, 5, 125–134, https://doi.org/10.5194/tc-5-125-2011, 2011.

Scambos, T. A., Bohlander, J. A., Shuman, C. A., and Skvarca, P.: Glacier acceleration and thinning after ice shelf collapse in the Larsen B
        Embayment, Antarctica, Geophysical Research Letters, 31, https://doi.org/10.1029/2004GL020670, 2004.

675   Shapero, D. R., Badgeley, J. A., Hoffman, A. O., and Joughin, I. R.: icepack: A new glacier flow modeling package in Python, version 1.0,
        Geoscientific Model Development, 14, 4593–4616, https://doi.org/10.5194/gmd-14-4593-2021, 2021.

Simmons, D. A. and Rouse, J. R.: Accelerating flow of the Brunt Ice Shelf, Antarctica, Journal of Glaciology, 30, 377–380,
        https://doi.org/10.3189/S0022143000006262, 1984.

Smith, B., Fricker, H. A., Holschuh, N., Gardner, A. S., Adusumilli, S., Brunt, K. M., Csathó, B., Harbeck, K., Huth, A., Neumann, T.,
680   Nilsson, J., and Siegfried, M. R.: Land ice height-retrieval algorithm for NASA's ICESat-2 photon-counting laser altimeter, Remote
        Sensing of Environment, 233, 111 352, https://doi.org/10.1016/j.rse.2019.111352, 2019.

Smith, B., Adusumilli, S., Csathó, B. M., Felikson, D., Fricker, H. A., Gardner, A., Holschuh, N., Lee, J., Nilsson, J., Paolo, F. S., Siegfried,
        M. R., Sutterley, T., and the ICESat-2 Science Team: ATLAS/ICESat-2 L3A Land Ice Height, Version 5. [September 2018 to Au-
        gust 2021. 65°S to 88°S], Boulder, Colorado USA. NASA National Snow and Ice Data Center Distributed Active Archive Center,
685   https://doi.org/10.5067/ATLAS/ATL06.005, date Accessed: 2021-2022, 2021.

Swinski, J. P., Shean, D., and Sutterley, T.: ICESat2-SlideRule/sliderule-icesat2: v1.4.3, https://doi.org/10.5281/zenodo.6600555, 2022.

Thomas, R. H.: The dynamics of the Brunt Ice Shelf, Coats Land, Antarctica, vol. 79, British Antarctic Survey, 1973.

U. S. National Ice Center: Iceberg A-81 Calved from the Brunt Ice Shelf in the Weddell Sea, https://usicecenter.gov/PressRelease/Iceberga81,
        accessed: 2023-03-01, 2023.

690   Walker, C. C. and Gardner, A. S.: Evolution of ice shelf rifts: Implications for formation mechanics and morphological controls, Earth and
        Planetary Science Letters, 526, 115 764, https://doi.org/10.1016/j.epsl.2019.115764, 2019.

Walker, C. C., Bassis, J. N., Fricker, H. A., and Czerwinski, R. J.: Structural and environmental controls on Antarctic ice
        shelf rift propagation inferred from satellite monitoring, Journal of Geophysical Research: Earth Surface, 118, 2354–2364,
        https://doi.org/10.1002/2013JF002742, 2013.

695   Walker, C. C., Bassis, J. N., Fricker, H. A., and Czerwinski, R. J.: Observations of interannual and spatial variability in rift propagation in
        the Amery Ice Shelf, Antarctica, 2002–14, Journal of Glaciology, 61, 243–252, https://doi.org/10.3189/2015JoG14J151, 2015.

Walker, C. C., Becker, M. K., and Fricker, H. A.: A High Resolution, Three-Dimensional View of the D-28 Calving Event From Amery Ice
        Shelf With ICESat-2 and Satellite Imagery, Geophysical Research Letters, 48, e2020GL091 200, https://doi.org/10.1029/2020GL091200,
        2021.

700   Wang, S., Alexander, P., Wu, Q., Tedesco, M., and Shu, S.: Characterization of ice shelf fracture features using ICESat-2 – A case study over
        the Amery Ice Shelf, Remote Sensing of Environment, 255, 112 266, https://doi.org/10.1016/j.rse.2020.112266, 2021.

Wang, S., Liu, H., Jezek, K., Alley, R. B., Wang, L., Alexander, P., and Huang, Y.: Controls on Larsen C Ice Shelf Retreat From a 60-Year
        Satellite Data Record, Journal of Geophysical Research: Earth Surface, 127, e2021JF006 346, https://doi.org/10.1029/2021JF006346,
        2022.

705   Zwally, H. J., Giovinetto, M. B., Li, J., Cornejo, H. G., Beckley, M. A., Brenner, A. C., Saba, J. L., and Yi, D.: Mass changes of the
        Greenland and Antarctic ice sheets and shelves and contributions to sea-level rise: 1992–2002, Journal of Glaciology, 51, 509–527,
        https://doi.org/10.3189/172756505781829007, 2005.